ACS NANO

Time-Resolved Fluorescence Imaging and Correlative Cryo-Electron Tomography to Study Structural Changes of the HIV-1 Capsid

Zaida K. Rodriguez,[▽] Jonathan R. Andino-Moncada,[▽] Sergey A. Buth,[▽] Atousa Mehrani, Ahinsa Ranaweera, Jincheng Shi, Leonardo R. Andrade, Satya Prakash Singh, Timothy S. Strutzenberg, Mariana Marin, Ricardo Guerrero-Ferreira, Hamid Rahmani, Danielle A. Grotjahn, Scott Stagg, Gregory B. Melikyan,* Dmitry Lyumkis,* and Ashwanth C. Francis*

Cite This: *ACS Nano* 2025, 19, 30902−30918

Read Online

ACCESS | Metrics & More | Article Recommendations | Supporting Information

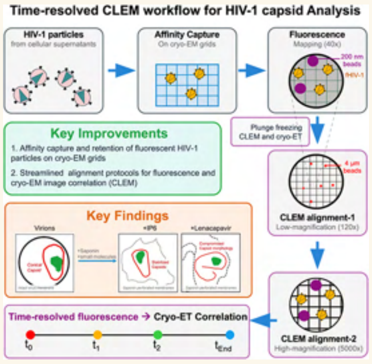

ABSTRACT: **The conical HIV-1 capsid protects the internal viral genome and facilitates the infection of target cells. Highly potent antivirals, such as the clinically approved drug Lenacapavir (LEN), block HIV-1 replication by changing the capsid structure and modulating its function. However, structural studies of the HIV-1 capsid, its disassembly, or stabilization by antivirals have been challenging. Here, we developed a correlative light and cryo-electron microscopy (CLEM) workflow to characterize HIV-1 capsid morphology, starting from a small volume of viral particles harvested from cellular supernatants. We report two critical improvements in sample preparation, namely, (1) affinity capture and retention of fluorescent HIV-1 particles on cryo-EM grids to enable mapping virus/capsid location prior to sample vitrification and (2) streamlined alignment protocols to subsequently identify and correlate regions of interest in fluorescence and cryo-EM images. These improvements enable a reproducible CLEM workflow to accurately locate capsids for cryo-electron tomography (cryo-ET) studies. Using this approach, we resolved ultrastructures of HIV-1 capsids treated with LEN and the cellular metabolite inositol hexaphosphate (IP6), revealing distinct modes of capsid lattice stabilization. Finally, using our CLEM workflow, we demonstrate the feasibility of correlating time-resolved fluorescence imaging of capsid disassembly to end point cryo-ET structures. These advances will facilitate in vitro structural studies to define the mechanisms of HIV-1 capsid stabilization and disassembly. The CLEM workflow developed here can also be extended to studying structural changes in other viruses in response to diverse stimuli.**

KEYWORDS: *HIV-1 capsid uncoating, IP6, lenacapavir, CLEM, cryo-ET*

HIV-1 particles are assembled at the plasma membrane of producer cells in the form of immature Gag and Gag-Pol polyprotein complexes.[1,2] During or shortly after viral egress from the cell surface, the HIV-1 protease (PR) cleaves the Gag/Gag-Pol precursor proteins at well-defined sites to release the individual domains of Gag (MA, CA, SP1, NC, SP2, and p6) and Pol (PR, RT, and IN), respectively. The released 24 kDa CA domain multimerizes into ~250 hexamers and 12 pentamers[3,4] to form a conical enclosure called the capsid, which protects the internal viral ribonucleoprotein (vRNP) complex. Together, the capsid and internal vRNP are called the viral core. The mature virion that contains a conical capsid morphology is structurally distinct from the immature form[5,6] and is responsible for the new infection of target cells.

Following its delivery into the cytoplasm, the capsid plays a dominant role in determining the outcome of virus infection.[7] Reverse transcription of the vRNA genome into complementary viral DNA (vDNA)[8,9] occurs within the confines of the capsid, which shields viral nucleic acids from host innate sensing.[10] The outer surface of the assembled capsid structure forms binding pockets that interact with numerous host proteins that facilitate transport of the HIV-1 core into the nucleus to establish infection.[11−18] The capsid thus serves to

Received: April 22, 2025
Revised: August 12, 2025
Accepted: August 13, 2025
Published: August 22, 2025

https://doi.org/10.1021/acsnano.5c06724

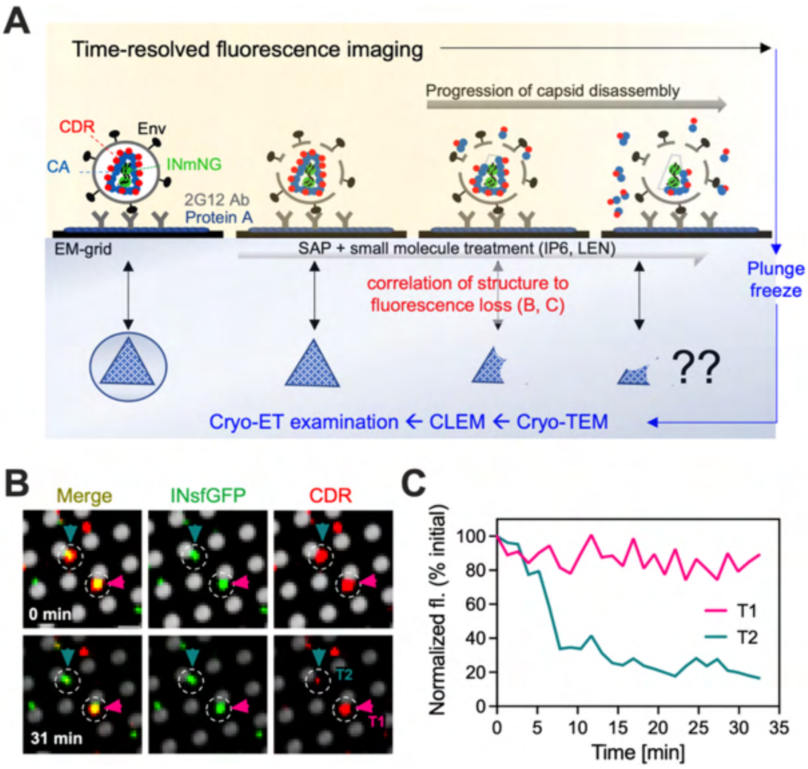

Figure 1. An in vitro assay to study HIV-1 uncoating by CLEM. (A) Schematics show fluorescent HIV-1 particles immobilized on cryo-EM grids using the 2G12 antibody-mediated affinity capture (see the main text and the section Materials and Methods). fHIV-1 is labeled with INsfGFP (green), which marks the vRNPs internal to the conical capsid shell (blue), and with the CDR (red) marker, which decorates the outer capsid surface. Following saponin (SAP) treatment, the viral membrane is permeabilized, and uncoating is initiated. Progression of uncoating is visualized by time-resolved imaging of CDR-loss. The goal of this study is to develop a CLEM workflow to correlate the loss of CDR visualized by time-resolved fLM to capsid structures by cryo-ET. (B) Representative initial and end-point images of a time-resolved imaging data set showing INsfGFP (green) and CDR (red) labeled cores captured on grids. Dashed circles identify cores that were tracked, and colored arrowheads identify presumably intact (pink) and fully uncoated (cyan) cores. Scale bar = 2 μm. (C) CDR fluorescence intensity traces showing HIV-1 cores uncoating to different extents corresponding to T1 and T2 cores in (B) over 31 min of imaging. See also Movie 22 related to (B) and (C).

both protect viral nucleic acids and deliver the vDNA to genomic sites for its integration into the host chromatin.

For productive infection, the capsid must disassemble to release the newly formed vDNA for integration into the host genome. The process of capsid disassembly is commonly referred to as uncoating.[7] When and where uncoating occurs during infection and how this process is regulated remain unclear. Based on the results of live-cell microscopy, several scenarios have been proposed, including loss of capsid integrity and cytoplasmic uncoating,[19] completion of uncoating at the nuclear pore,[20] and nuclear uncoating.[21−24] Notably, uncoating is intricately controlled and structurally complex. It is regulated by several processes, including reverse transcription, which is initiated in the cytoplasm[19,25] and can be completed in the nucleus,[21−23,26] capsid−host factor interactions,[14,25,27] and biophysical properties of the conical capsid lattice, such as its elasticity.[28] Due to the complex regulation of HIV-1 uncoating, the mechanisms through which it occurs remain debated.

Given its important roles in facilitating HIV-1 infection, capsid has emerged as a leading target for the development of antiviral compounds. Small molecule capsid-targeting inhibitors, such as PF74 and its derivatives,[29−31] including the clinically approved drug Lenacapavir (LEN)[32,33] and the LEN analogues GS-CA1 or GS-6207,[8,34] successfully block HIV-1 infection by increasing capsid stability and changing the rate of capsid uncoating.[25,34] The advent of LEN, which has also shown promise in pre-exposure prophylaxis prevention of new HIV-1 infections, and the development of newer capsid-binding drugs in the pipeline (https://www.croiconference.org/abstract/2711-2025/) highlight the clinical relevance for structural studies of capsid function.

We previously established a robust *in vitro* uncoating assay,[25] which relies on the incorporation of two fluorescently tagged proteins into assembling HIV-1 particles, namely a Vpr-integrase superfolder GFP (INsfGFP) to mark vRNPs[35] and the tetrameric cyclophilin A-DsRed (CDR) fusion protein that avidly binds to the outer capsid surface and reports capsid uncoating *in vitro* and in living cells.[20,25] In a typical *in vitro* assay (Figure 1A,B), fluorescent HIV-1 particles (hereafter termed fHIV-1) are immobilized to a surface and treated with saponin (SAP) to permeabilize the viral membrane and initiate the uncoating process. Time-resolved fluorescence imaging and single fHIV-1 tracking identify the extent of CDR-fluorescence loss to infer the extent and completion of capsid uncoating steps (Figure 1C).[25] The simple nature of this assay has found wide application for describing the effects of point mutations, including host factors and small molecule inhibitor interactions, on the *in vitro* stability of capsids.[14,25,34,36−40]

Here, we take advantage of this *in vitro* uncoating assay to develop a CLEM workflow that can spatiotemporally resolve the loss of the CDR marker and identify the associated capsid structures via cryo-electron tomography (cryo-ET) to provide

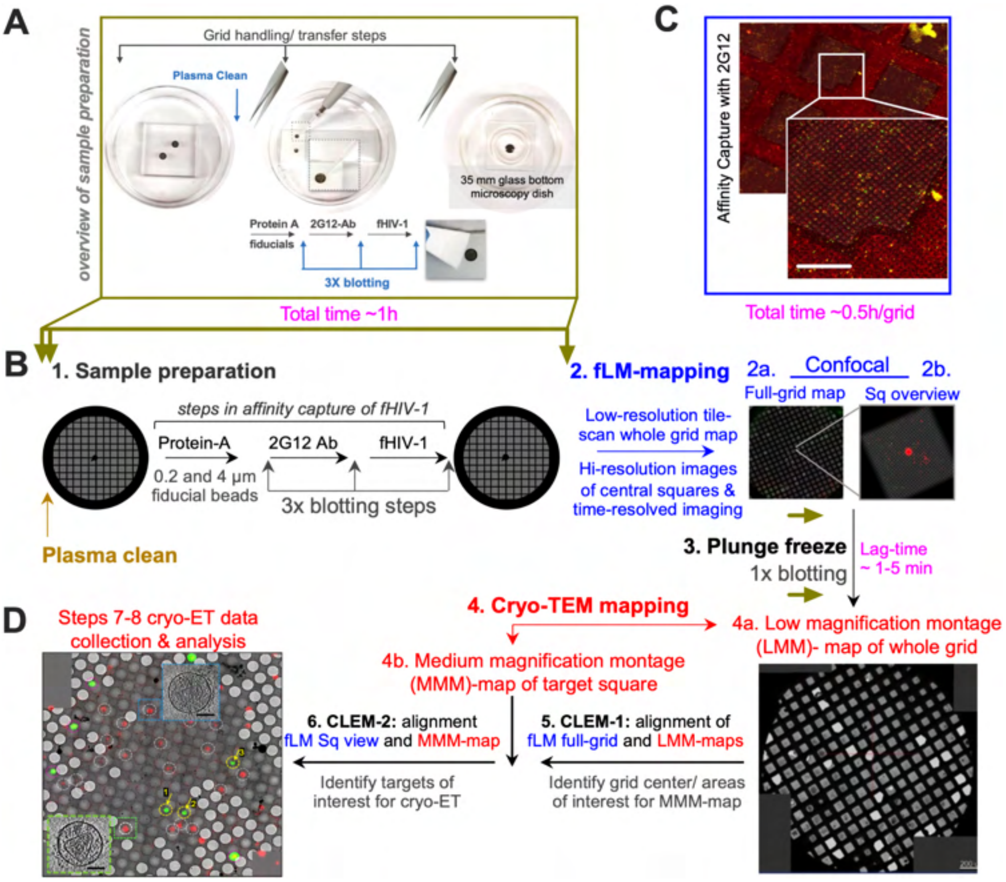

Figure 2. CLEM workflow for time-resolved studies. Overview of (A) sample preparation and (B) schematics of CLEM workflow steps 1−8 (see also Figure S1B and the section Materials and Methods). Golden arrows mark the small number of grid-handling steps that minimize grid damage, and the number of blotting steps in affinity capture is shown. The estimated time for completion of each step is annotated in magenta. (C) A zoomed-in image of an affinity-captured grid showing an even distribution of fHIV-1 puncta labeled with CDR (red) and INsfGFP (green). (D) An example of overlaid fLM, cryo-TEM, CLEM, and structural data (inset, steps 6−8) from a representative experiment. Scale bar in (C) 20 μm and insets shown in (D) 50 nm. The sample preparation (gray), fLM (blue), and cryo-TEM (red) steps are color-coded for clarity. Note: CDR and 200 nm beads are imaged using the same wavelength (ex/em 561/580), and 200 nm beads are not included in the example image shown in (C), which shows an even distribution of affinity-captured fHIV-1.

three-dimensional insights into the morphological changes occurring during uncoating. Notable improvements in this workflow include (1) the use of affinity capture to immobilize fHIV-1 particles onto cryo-EM grids and fluorescently map the location of virions and cores prior to plunge-freezing and (2) incorporation of differently sized fluorescent fiducial beads to facilitate multilevel CLEM and increase the likelihood of successful image correlation to identify regions of interest for cryo-ET data acquisition. The entire workflow from sample preparation through cryo-ET is highly reproducible, with an ~80% probability of accurately targeting capsids of interest.

Using this approach, we investigated the morphology of virions, including capsid structures that were obtained after virus membrane permeabilization with SAP. We illustrate key differences in capsid structures following treatment with LEN[8,34] and the cellular metabolite IP6.[8,41] In contrast to IP6, which predominantly stabilized a closed conical capsid structure, LEN stabilized an open capsid lattice that presumably lost its curved ends. Finally, as a proof-of-concept, we performed time-resolved fluorescence imaging of a dual-labeled HIV-1 core, which reports capsid integrity loss[19] and uncoating.[25] These studies demonstrate the feasibility of correlating an actively uncoating particle measured by fluorescence to an end point morphological characterization of the resulting structure via cryo-ET. Our CLEM workflow helps interrogate the mechanics of capsid stabilization and disassembly *in vitro* and provides complementary insights into HIV-1 capsid biology inside cells.

RESULTS

Workflow for Time-Resolved CLEM Studies of Fluorescently Labeled HIV-1 Particles. We set out to develop a cryo-CLEM workflow (Figure 2) that would enable capturing fHIV-1 particles and obtaining volumetric cryo-ET reconstructions of capsids on grids at discrete time points associated with dynamic changes to their morphologies. We modified the standard cryo-CLEM workflow (Figure S1A) to include fluorescence light microscopy (fLM) imaging to localize regions of interest (ROIs) prior to sample vitrification. Conventional strategies[42,43] employ fluorescence imaging under cryogenic conditions following sample vitrification to localize ROIs. However, cryo-fixation prior to fLM imaging means that users cannot follow dynamic events in real time. In other words, such approaches are not amenable to time-resolved fluorescence analyses, such as those that would provide contextual information on morphological changes to capsid dynamics over the course of minutes to hours (Figure 1C). Toward this goal, we made two specific improvements to

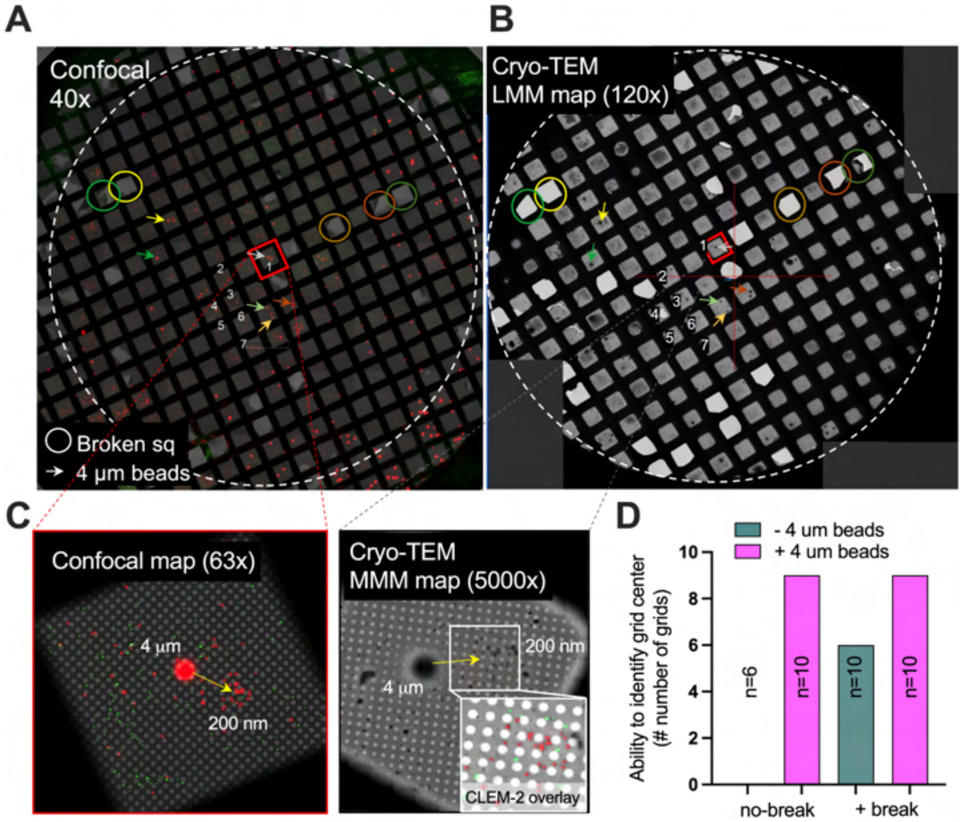

Figure 3. Incorporation of 4 μm fiducial beads improves the overall efficiency of the CLEM workflow. (A) fLM and (B) cryo-TEM overview montage maps of affinity-captured grids decorated with large 4 μm and small 200 nm fiducial beads (red). Colored circles identify broken squares, and colored arrows point to 4 μm fiducial beads used in the CLEM-1 alignment of the grid maps. For clarity, the cryo-TEM atlas in (B) is rotated to overlay the square numbers (#1−7) where high-resolution confocal data sets were collected. (C) Zoomed-in panels of (A and B)—high-resolution fLM image (left panels) and cryo-TEM MMM-map (right panels) of the central grid square #1 shown in A and B, show the distribution of fiducial beads (red in (A) and electron-dense dark puncta in (B)). The inset in right zoomed panels shows the CLEM-2 alignment of the grid square, with overlaid INsfGFP (green) and 200 nm bead (red) signals. (D) The ability to identify the grid center and orient the fLM- and LMM-TEM maps (CLEM-1 efficiency) was evaluated from different experiments containing either perfect grids (no break) or grids with broken squares, with (+) or without (−) 4 μm beads. The number of experiments (n) used in the analysis is indicated.

sample preparation, described below, to enable the new-CLEM workflow (Figure S1B).

Affinity Capture Immobilizes and Retains fHIV-1 Particles on Cryo-EM Grids. First, to evenly and reproducibly immobilize fHIV-1 on cryo-EM grids, we adapted an affinity capture procedure[44] (Figure 2A,B). In brief, plasma-cleaned EM grids were coated with a recombinant protein A (pA) from *Staphylococcus aureus*. The pA binds heavy chains of diverse antibodies with high affinity and exposes the antigen-recognizing variable domain to the sample for antigen capture. We then bound the broadly neutralizing 2G12 antibody, which targets a conserved epitope on the gp120 subunit of the envelope glycoprotein, to pA-coated grids and floated media containing HXB2 envelope-pseudotyped fHIV-1 for its capture. The sample preparation steps are shown in Figure 2A,B, and further details on this protocol are provided in the section Materials and Methods.

To enable time-resolved studies, we coupled the affinity capture approach to fLM imaging of the sample at room temperature prior to cryo-fixation. We reasoned that this protocol would enable the direct transfer of grids to cryo-TEM after plunge-freezing, followed by CLEM alignment of fLM/TEM images to identify targets for cryo-ET data collection (Figures 2B and S1B). Confocal imaging and analysis of the fHIV-1 particles affinity-captured on grids revealed a uniform distribution of well-separated single fluorescent puncta on individual grid squares (Figure 2C). By comparison, electrostatic binding of a 100× concentrated virus prep to poly-L-lysine-treated grids showed clusters of fluorescence on grids (Figure S2A, B).

Subsequent cryo-TEM analysis failed to successfully identify or correlate electron dense structures on PLL grids after vitrification. By contrast, affinity capture efficiently retained fHIV-1 particles on grids following vitrification and identified densities corresponding to fluorescently mapped virions on cryo-TEM micrographs (Figures 2D and S2C,D). These results suggest that affinity capture efficiently immobilizes and retains fHIV-1 particles on grids following vitrification and enables their identification in TEM through CLEM.

Differentially Sized Fiducial Beads Enable Multilevel CLEM for Morphological Characterization of fHIV-1 Particles. Second, to facilitate accurate fLM and cryo-TEM image alignment and identify discrete fHIV-1 particles for cryo-ET, we developed a multilevel CLEM procedure. The approach utilizes differentially sized fiducial beads and includes two levels of image correlation, namely, (1) 4 μm beads for full-grid low-magnification alignment, termed "CLEM-1", and

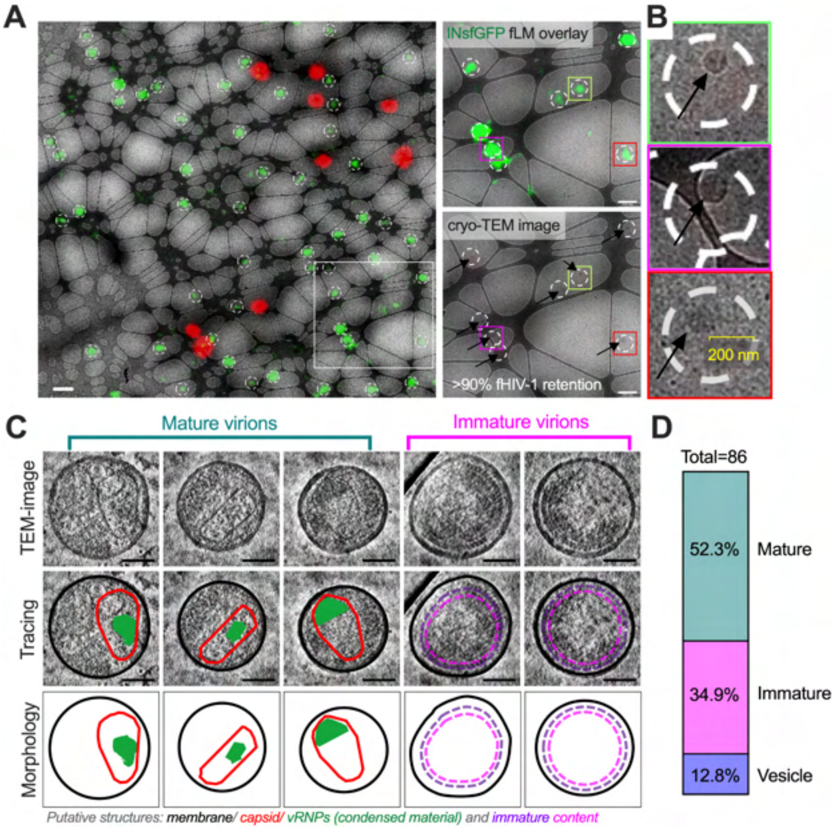

Figure 4. Affinity -captured fHIV-1 particles and 200 nm fiducial beads remain immobilized on cryo-EM grids. (A) Representative image showing CLEM-2 alignment of 200 nm fiducial beads (red) and the identification of fHIV-1 particles (green) on a lacey carbon film. A zoomed-in image from (A) with and without the fluorescence signal from overlaid fHIV-1 particles is shown in the right panels (top) and (bottom), respectively. Dashed circles highlight the location of fHIV-1 particles. (B) Zoomed-in view of boxed areas (A, right panels) showing circular structures representing virus particles. The fraction (>90%) of electron-dense structures of fHIV-1 particles and beads detected by fLM that was retained within the 200 nm radius dashed circles in (A) and (B) was determined from multiple experiments, shown in (A) (see also Figure 5F). (C) Examples of orthoslices from reconstructed structures by cryo-ET. (D) Quantification of the fraction of mature and immature viral particles, including vesicles in the cryo-ET data sets (n = 86), identified by the CLEM workflow and by cryo-ET data sets collected at the location of circular EM densities shown in (B). Tracing of substructures overlaid on TEM images (middle panel) and without overlay (bottom panel) is shown for clarity in (C). The scale bar in (A) is 2 μm, in zoomed-in images (right panels) is 500 nm, in (B) is 200 nm overlaid, and in (C) is 50 nm.

(2) 200 nm beads for high-magnification alignment of the grid square of interest, termed "CLEM-2" (Figure 2).

We evaluated the binding of the 4 and 200 nm beads to affinity capture grids by fLM and by cryo-TEM. The larger 4 μm beads were readily apparent within the fLM image maps and the cryo-TEM atlases collected by low-magnification montages (LMMs) of whole grids. The fLM image maps and the cryo-TEM atlases were accordingly used for CLEM-1 image alignment, yielding accurate identification of the grid center (Figure 3A,B). To quantitatively assess performance accuracy, we determined the success of CLEM-1 alignment using the identification of central grid squares between fLM and cryo-TEM as a readout (Figure 3C). CLEM-1 accuracy was assessed in 36 separate experiments, including 16 grids without 4 μm beads and 20 grids with 4 μm beads. Each of these grids could be further stratified into whether we did or did not observe broken squares in the fLM grid maps, which could be useful in CLEM-1 alignment.

In the absence of 4 μm beads and broken squares, it was challenging to align the fLM and cryo-TEM atlases. The formation of thick ice surrounding grid bars obscured the grid center (Figure S3A,B) and precluded accurate alignment of the fLM and cryo-TEM atlases in all experiments (n = 6/6, Figure 3D). However, if broken squares were present in the fLM grid maps, these aided successful CLEM-1 alignment of full-grid overview images in some cases (n = 6/10, Figure 3D), but not in other cases when broken squares were covered with ice (Figure S3). By contrast, the inclusion of 4 μm fiducial beads enabled their identification on the grid overview fLM and low-magnification cryo-TEM atlases (Figure 3A−C), leading to a highly efficient CLEM-1 image alignment and identification of the grid center, including regions of interest in nearly every experiment, irrespective of the presence of broken squares (n = 9/10 for both scenarios, Figure 3D).

We then collected medium-magnification montage (MMM) maps of the regions of interest, pertaining to grid squares that were fluorescently mapped by fLM. The locations of the smaller 200 nm beads detected within fLM square images were readily resolved as electron-dense dark punctates on the respective cryo-TEM MMM maps of the grid squares (Figure 3C). The 200 nm beads were then used in CLEM-2 image alignment to yield the coordinates of fHIV-1 particles for cryo-EM targeting (Figures 2D, 3C, 4A,B and S4A).

We next assessed the success of the CLEM-2 alignment and the ability to accurately target fHIV-1 puncta. Toward this goal, we first identified fluorescence spots corresponding to

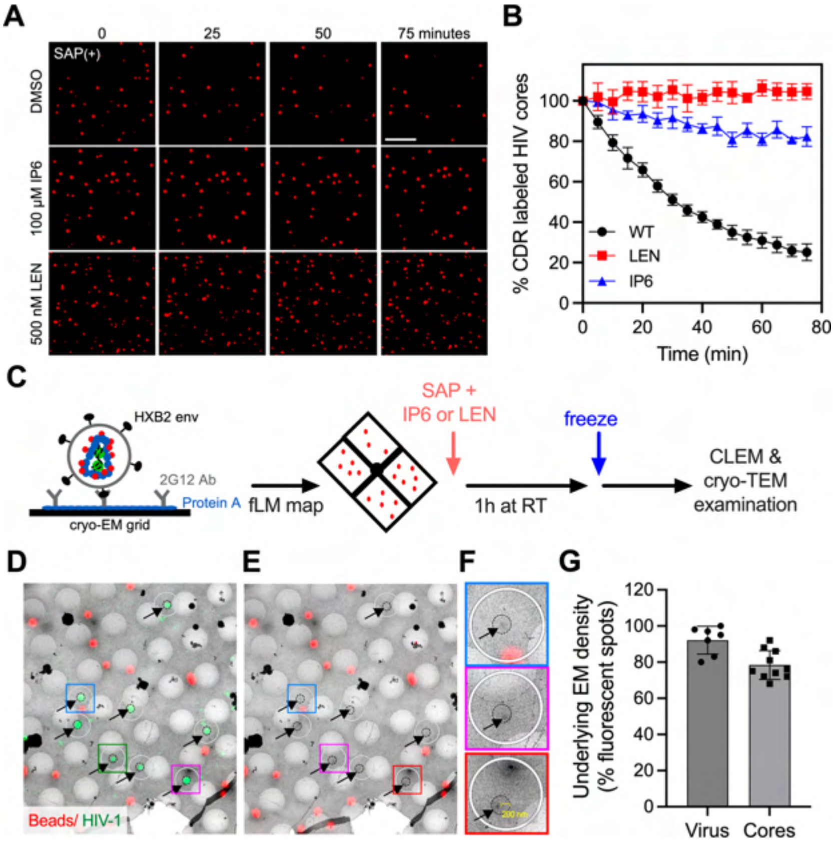

Figure 5. HIV-1 cores remain adhered to grids following virus membrane permeabilization. (A) Time-resolved imaging and (B) quantification of CDR puncta (red) loss from membrane-permeabilized virions (+SAP), treated with control DMSO, IP6 (100 μM), or LEN (500 nM). Data show the loss of the CDR marker in the presence of DMSO (control) and CDR retention during capsid stabilization by IP6 and LEN treatment. (C) Schematic of the CLEM workflow used to detect capsid structures. (D) A representative image showing CLEM-2 alignment of fLM and TEM MMM maps, showing 200 nm fiducial beads (red,; note the density of beads within overlaid images) and identification of fHIV-1 particles (green) on Quantifoil gold R2/1 grids. (E) Same as in (D) without the fHIV-1 overlay, and (F) a zoomed-in view of boxed regions in (E) to better visualize the densities (arrows; also see Figure S5Afor high-resolution images) underlying the location of the fHIV-1 signal (white circles) and within the 200 nm radius region marked by black dashed circles. (G) Quantification of electron densities of virus (shown in Figures 4A and S4A) and cores after (+SAP) virus membrane permeabilization that were identified within 200 nm of fluorescence signals of fHIV-1 particles by CLEM-2 image alignment (see also Figure S5B for precision of EM density localization with respect to fLM signals). Error bars indicate the mean and SEM from $n = 7$ (virions) and $n = 10$ experiments (cores, + SAP). The respective structures of virions from cryo-ET reconstructions are shown in Figures 4C and S4C and cores in Figure 6.

fHIV-1 particles and beads using a spot detector (see the section Materials and Methods) and then examined the CLEM-2 aligned images for underlying electron-dense structures. This analysis showed that densities corresponding to beads and virus-like particles characterized by a well-defined circular membrane (Figures 4A,B, and S4A) were all located within a 200 nm radius of the detected fluorescent spots (Figures 4B and S4B). These results on targeting accuracy are in agreement with prior reports.[45,46] In multiple experiments ($n = 7$), we noted that 100% of the 200 nm fiducial beads imaged by fLM were retained on grids, and >90% of fluorescent fHIV-1 signals were associated with discernible densities in the cryo-TEM image (Figure 4A).

Based on the identified fHIV-1 coordinates, we selected multiple locations for cryo-ET tilt-series acquisition. Following CLEM-2 alignment (Figure S4A,B), high-magnification single-plane cryo-TEM images resolved fHIV-1 substructures (Figure S4C). Similarly, cryo-ET tilt-series data collection ($n = 86$) at the location of fluorescence spots detected by CLEM, including at circular EM densities (Figure 4B), followed by tomogram reconstruction resolved the three-dimensional architectures of fHIV-1 virions at high magnification (Figure 4C and Movies 1−5). Tomogram analysis further classified HIV-1 substructures into mature virions containing classical conical-shaped capsids ($n = 45$), as well as immature virions with an intact Gag/Gag-Pol assembly ($n = 30$) (Figure 4D). In addition, a small fraction of the tomograms collected at circular EM densities (Figure 4B,D) without CLEM appeared as vesicle-like particles without a clear ultrastructure or morphology internal to the membrane densities, which are expected contaminants in virus supernatants containing media. These results show that affinity-captured fHIV-1 particles are stably immobilized on grids, enabling a robust correlation of fLM and cryo-EM images and the characterization of underlying structures.

IP6 and LEN Stabilize Morphologically Distinct Capsid Structures. Next, we asked if the CLEM workflow could resolve conically shaped HIV-1 capsids following virus membrane permeabilization, a step utilized for uncoating studies *in vitro* (Figure 1 and refs.[25,34,37,38], and 47). Toward this goal, we first determined the CDR fluorescence loss from cores following saponin (SAP) treatment. Since capsids are known to disassemble after virus membrane permeabilization, we utilized capsid-stabilizing small molecules, inositol

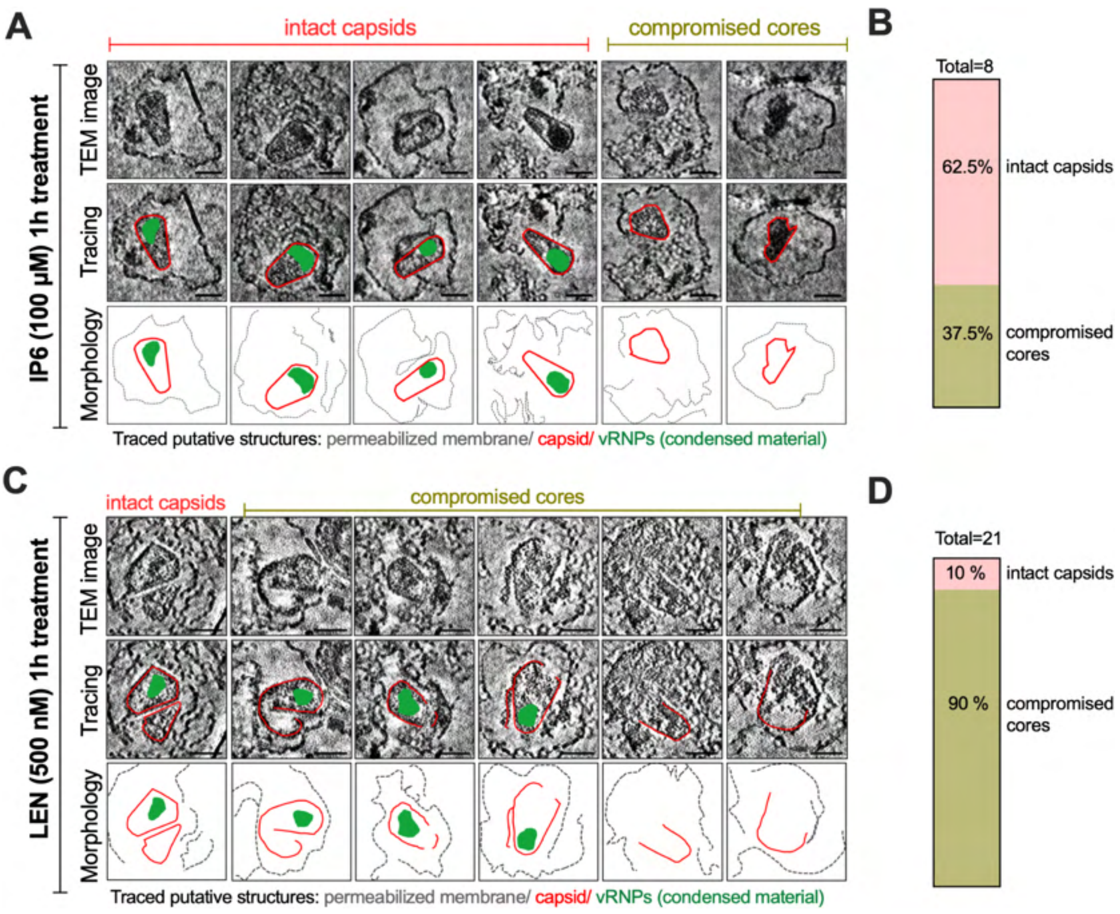

Figure 6. Ultrastructures of IP6 and LEN stabilized capsids. Examples of reconstructed cryo-ET tomograms depicting capsid morphology during treatment with (A) IP6 or (B) LEN identified by CLEM (Figure 5; additional tomographic snapshots for LEN-treated cores are shown in Figure S6B). The morphology of putative capsid structures (red), internal densities of vRNPs (green), and external permeabilized membrane densities (dashed gray lines) are highlighted by tracing on the 2D images. Densities of vRNPs in compromised structures could not be distinguished from those of debris and thus were not traced. The overlaid (middle panels) and traces alone (lower panels) are shown for clarity. Structures with full conical morphology were considered intact, whereas all other structures, including those that had partial conical features (visible broad or narrow ends), were considered compromised, as indicated in (A, B). Scale bars are 50 nm in A and B. Quantification of the fraction of intact and compromised cores (as shown in panels A and B) during (C) IP6 and (D) LEN treatment. The total number of tomograms analyzed is overlaid on each figure panel.

hexaphosphate (IP6, 100 μM), and the clinically approved inhibitor Lenacapavir (LEN, 500 nM)[8,32] in our experiments. Single virus imaging on glass coverslips confirmed that the half-time of capsid disassembly following membrane permeabilization was relatively short (~28 min, Figure 5A,B). As expected,[8,9,34,41,48] both IP6 and LEN stabilized the capsid lattice, as evidenced by a delayed/blocked CDR release (Figure 5A,B).

We examined the structures resulting from fHIV-1 capsid stabilization by IP6 and LEN via cryo-CLEM/cryo-ET. The distributions of fHIV-1 particles were mapped in the central grid squares, followed by the addition of IP6 or LEN (or DMSO), along with SAP to permeabilize the viral membrane and plunge-freezing for cryo-CLEM/ET analysis (Figure 5C). In contrast to the circular appearance of virions on cryo-TEM MMM maps (Figure 4B), SAP permeabilization yielded a blurry electron-dense substructure beneath fHIV-1 puncta (Figures 5D−F and S5A). Importantly, the electron density was retained within or near the borders of the 200 nm radius of CLEM-2 localization (Figures 5F and S5A), suggesting minimal displacement, if any, during SAP treatment and incubation with small molecules, as well as during plunge-freezing. Quantification of CLEM-2 efficiency (n = 10 experiments) showed that over ~80% of the fHIV-1 signals recorded with a spot detector were associated with an underlying electron density (Figure 5G). These results indicate that capsid substructures are retained at their locations, even after membrane permeabilization and plunge-freezing. To assess the localization precision of fluorescent objects on correlated EM images, we measured the distances between the centroids of fluorescent and respective EM densities seen as 200 nm electron-dense spheres for the fiducial beads used in CLEM-2 image alignment (Figure S5B). This analysis revealed that the mean localization precision for beads was within ~95 nm of the fluorescence objects (Figure S5B), highlighting the ability to accurately target viruses and cores by CLEM.

Morphological analyses following tomogram reconstruction showed that SAP permeabilization leads to markedly expanded and deformed membranes, which appear as discontinuous segments surrounding the viral cores (Figure 6A). However, SAP-mediated permeabilization does not completely dissolve the viral membrane, and cores are retained in their locations. We also noted the presence of immature particles containing permeabilized membranes in our data sets (Figure S6).

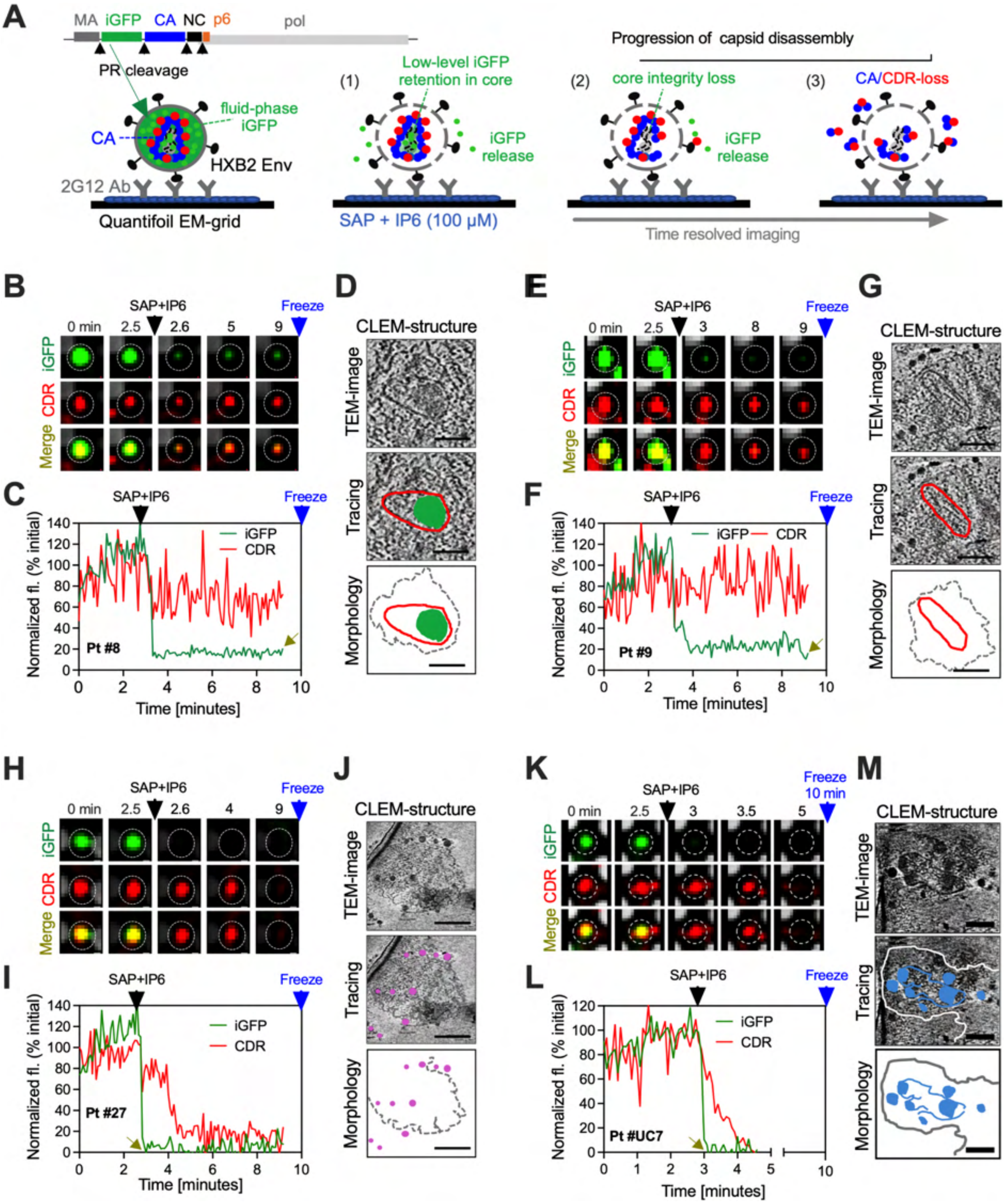

Figure 7. Proof-of-concept time-resolved CLEM studies correlate capsid uncoating dynamics to end point cryo-ET structures. (A) Schematics of fluorescent virus labeling with iGFP and CDR used in time-resolved CLEM experiments. The cartoon shows the affinity capture of fluorescent HIV-1 particles labeled with an iGFP fluid-phase marker. Three scenarios are depicted, including (1) the primary loss of iGFP that occurs during virus membrane permeabilization with SAP, followed by (2) a loss of capsid-entrapped iGFP molecules during the initial steps of capsid opening, and (3) subsequent loss of the CDR label that reports the disassembly of the remainder of the capsid structure. (B, E, H, and K) Experimental time-stamped images of fHIV-1 cores on grids showing iGFP and CDR fluorescence before and after SAP and IP6 addition at 2.5 min. (C, F, I, and L) Corresponding fluorescence intensity traces and (D, G, J, and M) orthoslices through reconstructed tomograms by cryo-ET showing the correlated capsid morphology. Data show a core that retained the capsid-entrapped iGFP signal and CDR fluorescence (B, C) appears intact with conical morphology (D), a core that lost the majority of its capsid-entrapped iGFP at 9 min but retained most of the CDR signals (E−G) appears as a tubular structure, and cores that completely lost iGFP and CDR signals (H−J and K−M) before plunge-freezing appear amorphous in structure. The time of SAP + IP6 addition (black arrow), the retention and/or complete iGFP loss (yellow arrow), and plunge-freezing (blue arrow) are overlaid on figure panels for clarity. Scale bars in D, G, J, and M are

Figure 7. continued

50 nm. The location of individual cores and trajectories on the CLEM-2 map (Figure S7) is overlaid on fluorescence traces in C, F, I, and L for clarity. See also related Figure S8 and Movies 17−21.

Tomographic analysis of mature cores treated with IP6 showed that most structures ($n = 5/8$) embedded within the permeabilized membranes were morphologically intact and conical in appearance (Figure 6A,B and Movies 6−11). There was also clear internal density within these cones, corresponding to the viral ribonucleoprotein complex (vRNPs). The rest of the analyzed cores ($n = 3/8$) exhibited an altered morphology (Figure 6B), which was distinct from immature particles (Figure S6A).

In contrast to the IP6-stabilized morphologically intact cores, LEN treatment led to significantly less numbers of intact conically shaped capsids ($n = 2/21$) and a greater number of partially conical cores with compromised morphologies ($n = 19/21$, Figures 6C,D, S6B and Movies 12−16). Notably, morphologically compromised cores were broken at the curved regions (both narrow and broad ends), resulting in an open capsid structure with sheets of the presumably hexameric capsid lattice, observed by other groups as well that used an analogue of LEN, GS-CA1.[8] These results support the reported different modes of capsid stabilization by IP6 and LEN. Collectively, these data highlight the practical application of our CLEM workflow to study the *in vitro* morphologies of native HIV-1 capsids derived from affinity-captured virions under different conditions.

Time-Resolved Fluorescence Imaging and Cryo-ET Studies of HIV-1 Capsid Disassembly. The efficient identification of HIV-1 capsids by the CLEM approach prompted us to explore the ability to characterize structures associated with the dynamics of viral uncoating. We asked if different states of uncoating visualized by time-resolved fluorescence imaging of single fHIV-1 cores could be correlated to end point capsid structures visualized by cryo-ET. We employed colabeled fHIV-1 particles with a fluid-phase GFP (iGFP) marker and the CDR capsid marker (Figure 7A). The iGFP marker is inserted between the matrix (MA) and capsid (CA) domains and incorporated into virus particles in the form of the Gag polyprotein during virus assembly.[49] Following viral proteolytic cleavage, the iGFP, along with the individual Gag domains, is released into the intraviral space of mature virions. A major fraction of the proteolytically processed iGFP molecules remains trapped between the conical capsid and the viral membrane and is released in a first step upon virus membrane permeabilization *in vitro*. Comparatively, a smaller subset of iGFP is trapped within the intact conical capsid shell, and this small fraction is released in a second step, once the capsid integrity is compromised (Figure 7A). This double-labeling approach enables studying capsid opening and subsequent capsid uncoating by measuring the stepwise loss of iGFP and CDR markers, respectively.

HIV-1 particles bearing HXB2 Env and labeled with the iGFP and CDR markers were affinity-captured onto cryo-EM grids, and grid overviews were mapped by fLM. We then performed time-resolved imaging to visualize the loss of iGFP and CDR after treatment with SAP in the presence of IP6 on the microscope stage. Time-resolved imaging was performed on 1 or 2 central EM grid squares every 5 s during a 9 min period, and the grids were immediately plunge-frozen in liquid ethane. We estimated the lag time between the cessation of time-resolved fLM-imaging and plunge-freezing to be ∼1 min. The frozen grids were stored in liquid nitrogen and transferred to cryo-TEM for CLEM studies.

We performed single-virus tracking on the recorded time-resolved movies to identify cores that showed loss of CDR or iGFP fluorescence and mapped their locations on the CLEM-2-aligned maps (Figure S7A,B). Subsequently, seven cores corresponding to three scenarios highlighted in Figure 7A were targeted for cryo-ET analysis. Following viral membrane permeabilization, which leads to the initial release of fluid-phase iGFP molecules, subsequent events were classified into three groups: (1) intact capsids ($n = 3$) were defined as puncta that retained CDR and capsid-entrapped iGFP markers at the end of imaging (Figure 7A (scenario (1)), B, C, and Figure S7, location pt #8, 14, and 21, Figure S8 A,B,D,E); (2) partial capsid disassembly/loss of integrity ($n = 2$) manifested by a major loss of capsid-entrapped iGFP but not the CDR marker (Figure 7A (scenario (2)), E, F and Figure S7, location pt #9 and 6, Figure S8G,H); (3) fully disassembled capsids ($n = 2$) seen as complete loss of iGFP and CDR (Figure 7A (scenario (3)), H, I, K,L and Figure S7, locations pt #UC7 and UC27). We then analyzed the resulting capsid morphologies via CLEM (Figure S7 and Movies 17−21) and cryo-ET tomographic reconstructions.

In agreement with the fluorescence-based interpretations, the core that retained both the capsid-entrapped iGFP and CDR markers (Figure 7B,C) tended to correlate with a presumably intact conical capsid morphology (Figure 7D and Movie 17). Two additional cores that retained integrity (Figure S8A,B,D,E) correlated to a tubular capsid structure (Figure S8C,F). Interestingly, the fHIV-1 particle ($n = 2$) that lost the majority of the core-entrapped iGFP fluorescence but retained nearly all CDR markers (Figure 7E,F and Figure S8G,H) also maintained a tubular morphology (Figures 7G, S8I, and Movie 18), although we could not definitively identify the structural defects. Finally, the two cores that lost both iGFP and CDR markers (Figure 7H,I,K,L) showed remnants of fully disassembled cores, similar to what was observed previously as viral RNP complexes[8] (Figure 7J and M, Movies 19 and 20). These proof-of-concept experiments demonstrate the utility of the affinity capture approach for time-resolved CLEM studies that correlate an end point cryo-EM structure to its immediately preceding uncoating dynamics.

DISCUSSION

The HIV-1 capsid must disassemble to allow for integration of the viral genome into the host chromatin. While the mechanisms underlying capsid disassembly remain unclear, *in situ* structural studies identified several examples of conically shaped capsids in the cytoplasm, at the nuclear pore, and inside the nucleus.[50,51] However, without understanding the structural intermediates and the end products of uncoating, identification of noncanonical capsid structures *in situ* is extremely challenging. Here, we developed a CLEM workflow and combined it with time-resolved fLM imaging and cryo-ET to demonstrate the feasibility of identifying uncoating intermediates of the HIV-1 capsid *in vitro*. This workflow will be directly useful for *in vitro* studies of HIV-1 uncoating and can be extended to *in situ* studies in the future.

Immobilization of fHIV-1 particles onto cryo-EM grids via affinity capture greatly improves our ability to reliably image the samples on grids prior to plunge-freezing while retaining virions and cores for cryo-TEM studies. As with the newer affinity grid technologies,[52,53] the advantages of affinity capture of fHIV-1 particles include avoiding the production of large volumes of virus-containing cellular supernatants and time-consuming high-speed ultracentrifugation steps, as well as having the ability to work with unconcentrated or mildly concentrated samples to remove contaminants in the media. The affinity capture approach described here can be expanded to other viruses, subviral structures, extracellular vesicles, and macromolecular assemblies. Comparable high-affinity antibodies, like 2G12, which we leveraged here, could be employed to capture other viruses. Future studies will be needed to address whether the core stability of virions pseudotyped with HXB2 envelope glycoproteins differs from that of replication-competent virions and whether antibodies that capture pseudoviruses by binding to the envelope glycoproteins can modify capsid uncoating.

Inclusion of differently sized fiducial beads into the workflow overcomes problems associated with the alignment of fLM and LMM map cryo-TEM grid overview images. The larger 4 μm beads facilitate efficient CLEM-1 image alignment (Figure 3D), which helps to identify the location of grid squares of interest. The 4 μm beads were selected because of their visibility within LMM maps, collected at 100−120× magnification on cryo-TEM. We surmise that smaller beads (1−2 μm), which were not tested in this study, may also be visible on LMM maps and can be incorporated into the CLEM workflow to facilitate CLEM-1 image alignment. The smaller 200 nm beads are not visible within the LMM maps, but they are visible within MMM maps to enable CLEM-2 image alignment and localization of capsids defined by discrete structural stabilities for high-resolution cryo-ET. Collectively, the inclusion of 4 μm beads increased the likelihood of success of the new CLEM workflow to ~80% (Figures 2, 3D, and 5G), and 200 nm beads enable the localization of virus particles and capsids with high precision. The high level of success is essential for the efficient coupling of time-resolved fLM data to structures obtained by cryo-ET.

Of note, affinity capture combined with multilevel CLEM allowed us to image the sample by fLM prior to plunge-freezing. This avoids time-consuming procedures and potential ice contamination issues associated with the intermediate cryo-fLM imaging step used in conventional workflows.[42,43,45] In addition to identifying the location of virus/capsid samples, the practical applications of imaging prior to plunge-freezing include having the ability to (1) perform time-resolved studies to identify capsids at different uncoating states, (2) identify the relevant mature virus cores based on the release of a fluid-phase marker following virus membrane permeabilization for cryo-TEM studies, and (3) obtain contextual information regarding the dynamics associated with an end-point structure seen by cryo-EM. In the future, fluorescently labeled host factors and small molecules can be included in the time-resolved imaging setup to bind affinity-captured cores and enable identification of the associated capsid structures during these interactions.

Through the above improvements, we could simultaneously resolve uncoating dynamics of the HIV-1 capsid and correlate these dynamics to provide contextual information to an end point cryo-EM structure (Figure 7). We demonstrate this application through proof-of-concept time-resolved CLEM, which correlated fluorescence intensity to end point cryo-EM structures. While we utilized iGFP-labeled virions for time-resolved studies here, the capsids derived from these viruses are known to be pleomorphic and show different profiles of fluid-phase iGFP release.[54] More experiments will be needed to clarify whether the identified morphologies, including the tubular structures associated with capsid-entrapped iGFP-loss, are representative events or isolated occurrences. Further improvements in fluorescent HIV-1 labeling, including newer fluorescent CA-tagging approaches[21,24] and improved probes, may facilitate more precise interpretation of fLM studies.

Recent work exploring capsid structures inside cells[55,56] identified morphological and volumetric changes to capsids during HIV-1 nuclear entry. Of note, Hou et al.[56] found that, in comparison to conical capsids, an overwhelmingly large number of tubular capsid structures were found at the nuclear pore (~3-fold), and an even higher fraction (~20-fold) was imported into the nucleus in a permeabilized cell system. These data sets provide evidence of the large statistical occurrence of tubular capsid entry into the nucleus of cells. Our finding that two cores (Figures 7E−G and S8G−I) that lost the majority of the iGFP marker are tubular in structure is intriguing. However, given the limited available data and the proof-of-concept nature of the current work, we refrain from drawing further conclusions about tubular capsid structures, including as they relate to capsid integrity loss.

Our results add to the growing evidence for capsid stabilization by IP6 and LEN[8,34] and provide novel insight into their different modes of action.[8,34] In contrast to IP6, which stabilizes a morphologically intact capsid structure, 500 nM LEN compromised the overall conical capsid morphology over 1 h of incubation. Interestingly, LEN-stabilized capsids were characterized by inwardly curved sheets that contain small defects that begin within the highly curved regions of the capsids. These observations are consistent with LEN-induced capsid breakage described by a variety of assays, including cryo-EM of GS-CA1-treated cores,[8] total internal reflection fluorescence microscopy of content leakage from capsids treated with LEN,[48] and, more recently, by negative-stain EM.[57] This collective evidence provides complementary insights into the mechanism of LEN-induced hyperstabilization of the lattice and capsid breakage.

While our studies demonstrate how capsids break when they are treated with high concentrations of inhibitor (500 nM LEN, which is ~100-fold greater than its clinically relevant IC50 values), similar observations of lattice stabilization and capsid breakage at more clinically relevant 1−100 nM LEN concentrations were also made recently by other groups.[57] Of note, LEN-induced capsid breakage occurs specifically at the curved regions of the capsid that is occupied by CA pentamers (Figure 6C).[8,57] It will be useful to determine whether LEN's potency in disrupting capsid morphology correlates with the inclusion of pentameric-CA species into its lattice. In future studies, our CLEM workflow could be used to provide more mechanistic insights into capsid stabilization by the combinatorial effects of IP6 and/or LEN. As LEN is used in the clinic,[32,33] it would be particularly interesting to employ the assay to study the effects of drug-resistant mutations on core architecture and morphology.

Limitations and Perspectives for Future Development. Affinity capture and CLEM enabled the efficient targeting of virions for cryo-ET structural analysis and resolved mature and immature virions. The INsfGFP and CDR dual-labeled fHIV-1 particles utilized in this study can report capsid uncoating *in vitro*;[25] however, they do not allow us to distinguish the mature and immature forms in virions. In fact, a third of our cryo-ET data sets (Figure 4C,D) contained immature HIV-1 particles. The ability to focus cryo-ET experiments exclusively on mature virions is desirable for the structural characterization of capsids. Since iGFP molecules are released only from mature, proteolytically processed cores, colabeling with HIV-GagiGFP and CDR helps to distinguish the locations of mature and immature virions for cryo-EM targeting through preceding time-resolved fLM and CLEM. Newer HIV-1 labeling approaches[58] that can use Förster resonance energy transfer (FRET) to discern the mature and immature forms could also be leveraged for these purposes.

By using SAP to permeabilize viral membranes, we observed a discontinuous, segmented membrane morphology surrounding capsids, suggesting that SAP does not fully dissolve the viral membranes. Alternative strategies for dissolving the viral membrane include the use of pore-forming proteins, such as perfringolysin O, to perforate viral membranes utilized in other studies.[13,54,59] Pore-forming proteins assemble ring-shaped pores in membranes, which permit the passage of small molecules and proteins, while the viral core is retained inside the membrane, enabling visualization of capsid dynamics over time. Future quantitative studies that employ time-resolved imaging and cryo-ET to compare the different methods of membrane permeabilization would be useful to delineate optimal workflows for the high-resolution reconstructions of capsids.

We acknowledge that the current workflow can miss events occurring between the cessation of time-resolved imaging and plunge-freezing. Innovations in microfluidics hardware for sample visualization and on-stage automated plunge-freezing, as, for example, reported by Fuest et al.,[60] as well as software development to provide real-time feedback and automate the plunge-freezing of specimens in response to fluorescence signals, may be needed to further streamline uncoating studies.

This study presents "proof-of-concept" morphological snapshots of virions that are evident under various treatments and conditions *in vitro*, including isolated occurrences of capsid structures associated with fluorescence loss. Our cryo-ET workflow presented here could be immediately leveraged to identify capsid structures during endogenous reverse transcription (ERT)[8] to resolve more physiologically relevant structural intermediates during uncoating. However, whether the structures identified *in vitro* reflect the pathways and intermediates of cellular uncoating remains unclear. Current limitations in both targeting accuracy and throughput for *in situ* CLEM remain a bottleneck for gaining large-scale statistical insights into capsid morphologies inside cells. To this end, the structures we identify using the *in vitro* CLEM approach may serve as references to cross-verify their relevance inside cells. Joint efforts to acquire and cross-validate data using both *in vitro* and *in situ* CLEM will collectively advance our understanding of this important but still poorly understood step in the HIV-1 replication cycle.

MATERIALS AND METHODS

Cell Lines and Plasmid Reagents. HEK293*T*/17 (from ATCC, Manassas, VA) were grown in a complete high-glucose Dulbecco's Modified Eagle Medium (DMEM, Mediatech, Manassas, VA) supplemented with 10% Fetal Bovine Serum (FBS, Sigma, St. Louis, MO), 100 U/mL penicillin-streptomycin (Gemini Bio-Products, Sacramento, CA), and 0.5 mg/mL G418 sulfate (Mediatech, Manassas, VA). The plasmid vectors encoding the HIV-1 backbone—pR9ΔEnv, pHIV-GagiGFPΔEnv, and pHIVeGFPΔEnv—as well as the CypA-DsRed (CDR) and pVpr-IN-superfolderGFP (INsfGFP) are described previously.[15,20,25] The plasmid pHXB2-rev encoding the HXB2-envelope glycoproteins was a kind gift from Massimo Pizzato (University of Trento, Italy). All plasmid sequences were verified by Sanger sequencing (Genewiz, USA).

Pseudovirus Production and Characterization. Fluorescently labeled pseudoviruses were produced and characterized as described previously[20,25] using the JetPrime Transfection reagent (VWR, Radnor, PA) according to the manufacturer's protocol. Briefly, 2 μg of plasmids expressing the HIV-backbone (pR9ΔEnv, pHIVeGFPΔEnv, or pHIV-GagiGFPΔEnv) and 0.5 μg of envelope glycoproteins pHXB2-Rev were cotransfected along with 0.8 μg fluorescently tagged IN (Vpr-INsfGFP) and 0.5 μg CypA-DsRed capsid marker (CDR) plasmids in 200 μL jetPrime buffer and 6 μL jetPrime reagent into HEK/293T cells maintained in complete DMEM media in a well of 6-well plates (corning). After 6 h of transfection, the medium was replaced with 2 mL of fresh complete DMEM without phenol red. After further incubation for 36 h at 37 °C, 5% CO_2, viral supernatants were collected, filtered through a 0.45 μm filter, and quantified for the RT activity (RTU) measured using the SG-PERT protocol.[61] Alternatively, a low-speed centrifugation of 2 mL of viral supernatants by the Lenti-X concentrator (Takara Biosciences) was performed as per manufacturer's protocol to remove serum from the media. In this case, the pellet was resuspended in 200 μL of PBS (10× concentration) and stored until further use.

Cryo-EM Grids Used in This Study. Different kinds of cryo-EM grids were used in this study, including 200 mesh (1) R2/1 Quantifoil Holey Carbon gold grids (EMS, Hatfield, PA, Q2100AR1), (2) R1/4 Quantifoil Holey Carbon gold grids (EMS Q210AR-14), (3) R2/1 Quantifoil Holey Carbon gold grids with a continuous layer of 2 nm carbon film (EMS Q2100AR1-2 nm), (4) gold grids with lacey carbon with a continuous layer of 2 nm carbon film (EMS LC200-Au-CC), and (5) copper grids with lacey carbon with a continuous layer of 2 nm carbon film (EMS LC200-Cu-CC). We also tried finder grids (EMS G200F1-Au) in some experiments to evaluate the feasibility of CLEM. The grids were stored in a vacuum-contained chamber until the day of sample preparation. We note that all of the above grids work perfectly to immobilize virions onto the carbon film by the affinity capture method described below, albeit virions and cores are excluded from the holes (grids 1 and 2). We therefore purchased grids with a 2 nm carbon film covering the holes (grids 3–5) and used these in some of our studies (Figures 3–6). We note that the use of 2 nm carbon film-coated grids greatly facilitated particle capture directly over the holes, which is advantageous for high-resolution cryo-ET imaging.

https://doi.org/10.1021/acsnano.5c06724
ACS Nano 2025, 19, 30902−30918

Affinity Capture of fHIV-1 Particles and Beads on EM-Grids. We minimized the number of times the EM grids came in contact with the forceps, as shown in Figure 2A. Grid handling step 1: for every experiment, the grids were either (1) glow-discharged for 30 s at high radio frequency (RF) settings using the Harrick-Plasma PDC-32G instrument (Harric Plasma, Ithaca, NY) or (2) plasma cleaned with a Gatan Solarus 950 plasma cleaner (Gatan, Pleasanton, CA) for 20 s with an O_2/Ar plasma. Grid handling step 2: glow-discharged or plasma-cleaned grids were then moved to a parafilm-coated glass slide (3" × 1", 1 mm thickness) placed in a 10 cm tissue culture dish for sample preparation.

To prepare affinity grids, 5 μL of a Protein A-bead mixture (see below) was applied directly to the glow-discharged EM grid and incubated for 15 min. The Protein A-bead mixture was prepared by mixing 40 μL of 100 μg/mL Protein A solution (Sigma-Aldrich, St. Louis, MO, #P6031) with 7.5 μL of solution containing 1:200 dilution of 4 μm fluorescent (580/605 nm) sulfate beads (Thermo Fisher Scientific, Waltham, MA, F8858) and 2.5 μL of 1:1000 dilution of 0.2 μm fluorescent (660/680 nm) carboxylate beads (Thermo Fisher Scientific, F8807). Following Protein A/bead incubation, the grid was rigorously blotted from the side 3× with a grade 4 Whatman filter paper (GE Healthcare, Chicago, IL, #1004) by adding 5 μL of PBS intermittently between blotting steps, as shown in Figure 2A. A 5 μL portion of a 1:20 dilution of 2G12 antibody (NIH ARP 1476, obtained through the NIH HIV Reagent Program) was then added to the grids and incubated for 10 min to allow antibody adsorption to the Protein A-coated grid surface. The excess and unbound antibodies were washed away by blotting 3× with Whatman filter paper as described above. Finally, 5 μL of viral supernatant was added to the grids and incubated for 20 min for affinity capture of fHIV-1 particles. The unbound virus particles were additionally washed away by blotting 3× with Whatman filter paper by intermittently applying a drop of 5 μL of PBS. The rigorous blotting steps ensured that only affinity-captured fHIV-1 particles were imaged under the fLM. Grid handling step 3: the grid was then moved into a 35 mm microscopy dish (MatTek, Ashland, MA, P35GCOL-1.5-14-C) and maintained in 100 μL PBS for confocal imaging. Because the grids are rigorously blotted (~9×) during sample preparation, we expected that the tightly bound fHIV-1 particles are unlikely to be displaced by the necessary final back-sided gentle blotting of grids during sample plunge-freezing (*1×, step-3 shown in* Figure 2B). We estimate the entire sample preparation steps to be completed within ~1 h.

Confocal Imaging and Fluorescence Analysis. Confocal imaging was performed on a Zeiss LSM880 (Carl Zeiss, Oberkochen, Baden-Württemberg) or a Leica SP8 confocal microscope (Leica Microsystems, Wetzlar, Hesse) using a C-Apo 63x/1.4 N.A. oil objective. The grids were imaged using the 488, 561, and 633 nm laser lines to visualize INsfGFP or iGFP fluorescence (Em: 502−550 nm), CDR and 4 μm fiducial beads (Em: 572−640 nm), and 200 nm fiducials (Em: 642−700 nm), respectively, using hybrid HyD (Leica) and GaSP-PMT detectors (Zeiss). A wide-field T-PMT image of the grid was collected sequentially with the indicated laser lines in parallel. Images were first collected in the tile-scanning mode at 240−360 nm pixel sizes to map the entire grid (Atlas). Subsequently, the central grid squares (~2−16) were imaged at higher magnification using 4× line averaging and 120 nm pixel sizes. The pixel dwell times were 1.54 μs, and the frame size was set to either 512 × 512 or 1024 × 1024 pixels. Mapping of the entire grid atlas (1−2 min per grid), including the high-magnification imaging of central grid squares (40 s−1 min per square) at room temperature, was estimated to be between 15 and 20 min. Once virus adherence or capsid disassembly was imaged, the grids were manually transferred into a cryo-plunging system (see below) and plunge-frozen. Plunge-freezing was done immediately after fLM imaging and/or after 1 h of treatment with saponin (Millipore Sigma, Cat. # 558255) (SAP, 100 μg/mL) in the presence or absence of small molecules: 100 μM IP6 (TCI, Cat. # P0409) or 500 nM of LEN (MedChemExpress, Cat. # HY-111964).

For time-resolved studies, the location of fHIV-1 particles on the grids was mapped as described above. Then, time series images were collected to measure iGFP and/or CDR loss after virus membrane permeabilization with SAP in the presence of 100 μM IP6. Single-plane time-lapse images of 1−4 central squares were acquired every 5 s for a period of 9 min, and the sample was plunge-frozen immediately in a precooled CryoPlunger3 (CP3) device (Gatan). The time lag from imaging to plunge-freezing was ~1 min. The distribution of fluorescently tagged single virus particles and beads on the confocal and TEM images was analyzed offline and aligned by ec-CLEM[62] using ICY image analysis software. Spot tracking was employed to visualize the rate and extent of iGFP or CDR fluorescence loss from single virus puncta, and the resulting fluorescence intensity traces were plotted on Prism (GraphPad) graphing software. Once coordinates of the intact and uncoating capsids (Figure S7) were identified on the CLEM-aligned images, these were used for cryo-ET data collection.

Sample Vitrification. Prior to sample vitrification, a 5-μL aliquot of 10 nm gold nanoparticles (EMS, BSA Gold Tracer, 25486) was applied to each grid to be used later for image alignment in the 3D tomographic reconstruction process. TEM grids were vitrified by rapid plunging in liquid ethane using either a semiautomated CryoPlunger3 (CP3) device (Gatan) or a Vitrobot Mark IV (Thermo Fisher Scientific). Samples were vitrified using a back-sided blotting scheme for a duration of 5 s prior to plunging into liquid ethane. The humidity in the chamber was recorded between ~85 and 95% during freezing, while the temperature of liquid ethane was maintained at −180 °C. Following plunge-freezing, the grids were transferred into a grid storage box and stored under liquid nitrogen until the cryo-TEM data collection session. The grids that were imaged on the Titan Krios were clipped using an AutoGrid sample carrier (Thermo Fisher Scientific).

Cryo-TEM Imaging, CLEM, and Cryo-ET Data Collection. Cryo-TEM imaging was performed using a 200 keV JEOL JEM-2200FS or a 300 keV Titan Krios microscope (Thermo Fisher Scientific) using the SerialEM software, as described below:

200 keV JEOL JEM-2200FS data collection: cryo-grids were transferred to a Gatan 914 high-tilt holder maintained at −178 °C. Cryo-grids were imaged with a JEOL JEM-2200FS 200 keV field emission gun transmission electron microscope equipped with an in-column Omega energy filter (slit width: 20 eV), an UltraScan US4000 CCD (Gatan), and a DE-20 direct electron detector (Direct Electron, San Diego, CA). Grid overview, low-magnification maps (LMMs), and grid square medium-magnification montage (MMM) maps were collected at 100× and 5,000× nominal magnification, respectively, using a Gatan US4000 camera. Tilt series were

acquired at 10,000× nominal magnification (calibrated pixel size of 6.14 Å at the level of the specimen) at −4 to −8 μm defocus using a DE-20 detector in movie mode. Tilt series were recorded in the −60° to 60 ° angular range using a bidirectional scheme starting from 0° with a 2° tilt increment. The total electron dose per tilt series was in the range of 120–150 $e^-/Å^2$. Data collection was carried out using the SerialEM software.[63]

300 keV Titan Krios data collection: cryo-grids were transferred to a 300 keV Titan Krios microscope (Thermo Fisher Scientific) equipped with a K3 direct electron detector (Gatan). LMM maps were collected at 135× magnification, and MMM maps of grid squares were collected at 3600× magnification. Following CLEM and sample identification, cryo-ET tilt-series data sets were collected at a nominal magnification of 53,000× (pixel size 1.68 Å) with a defocus range of −2 to −5 μm. A 100 μm objective aperture was inserted, and a BioQuantum energy filter with a 20 eV-wide slit was used throughout data collection. Using PACE-tomo[64] in SerialEM, tilt series images were collected automatically. Each tilt series was acquired with a dose-symmetric scheme in tilt ranges of −60° to +60° with an increment of 3°. The total dose was ~120 $e^-/Å^2$ with a dose rate of 3 $e^-/Å^2$/sec.

Multi-level CLEM Image Alignment and Efficiency Calculations. CLEM-1 (grid overview fLM vs LMM TEM maps) and CLEM-2 (high-resolution fLM vs MMM TEM maps) alignments were carried out in the ec-CLEM.V2 plugin[62] within the ICY bioimaging software suite. 4 μm beads, a grid center mark, and grid squares with torn carbon (when available) were used as reference points for CLEM-1 correlation. 0.2 μm beads were used for CLEM-2 correlation. After image alignment, regions of interest were identified and transferred to Serial EM for the tilt-series data collection.

CLEM-1 efficiency was calculated manually based on successful experiments in correlating LMM and fLM grid overview maps (Figure 3C). CLEM-2 efficiency was calculated as follows: (1) first, the fLM square overview and corresponding MMM maps were aligned via the ec-CLEM plugin; (2) the aligned images have an extra channel corresponding to the MMM map; (3) fluorescent spots were detected using a spot detector plugin as described previously;[15,65] (4) the spots were exported as ROIs, which were resized to a 400 nm diameter within ICY analysis software; and (5) the electron densities below the resized ROIs were examined manually by 2 or more operators. The efficiency for each experiment was additionally calculated by the fraction of 200 nm fluorescent beads and fHIV-1 signals present on the fLM square overview images that were retained as electron-dense objects on MMM maps. Beads appear with perfectly circular electron densities, and virus/cores were estimated based on circular or blurry appearances as described in the main text and figures (Figures 4 and 5, S4 and S5). The fraction of correlated locations with electron densities from each experiment is plotted in Figure 5F. The distances between the centroid of fluorescent spots and the respective underlying electron density were measured manually and plotted to derive the precision of CLEM-2 localization (Figure S5B).

Tomogram Reconstruction, Segmentation, and Analysis. Data sets in all initial studies (Figures 2–6), including time-resolved studies (Figure 7), were collected using the JEOL JEM-2200FS 200 kV at the *Robert P. Apkarian Electron Microscopy Core Facility at Emory University* or using the Titan Krios 300 keV instrument in *Biological Sciences Imaging Resource and the Southeastern Center for Microscopy of MacroMolecular Machines (SECM4) at Florida State University.* Data sets (Figures 5 and 6 and S4) corresponding to IP6 and intact virions were collected on a 300 keV Titan Krios microscope *at the New York Structural Biology Center*. These data sets were collected at a nominal magnification of 19,500× (pixel size of 4.51 Å) with a defocus range of −2 to −5 μm. Alternatively, data sets for the LEN in Figure 6 were collected at Scripps Research (La Jolla, CA). Data sets were collected at a nominal magnification of 53,000× (pixel size of 1.68 Å) with a defocus range of −2 to −5 μm.

200 keV JEOL JEM-2200FS data processing: all movie frames were dark-subtracted and gain-normalized on the DE Server (Direct Electron), followed by frame alignment and summing using RELION.[66] Tilt series were aligned and binned three times, and tomograms were reconstructed with eTomo and IMOD[42] employing the weighted back projection algorithm. Reconstructed tomograms and single images were visualized in 3dmod.

300 keV Titan Krios data processing: all movie frames were preprocessed, specifically contrast transfer function estimation and motion correction, in Warp and aligned using AreTomo.[67] Alignment data were fed back to Warp for tomogram reconstruction with weighted back projection into four times binned tomograms. Tomogram visualization and tracing were performed on deconvoluted tomograms generated from Warp.[68,69]

ASSOCIATED CONTENT

Supporting Information

The Supporting Information is available free of charge at https://pubs.acs.org/doi/10.1021/acsnano.5c06724.

Back-projected cryo-ET reconstruction of mature virions pertaining to Figure 4C (Movie S1) (AVI)

Back-projected cryo-ET reconstruction of mature virions pertaining to Figure 4C (Movie S2) (AVI)

Back-projected cryo-ET reconstruction of mature virions pertaining to Figure 4C (Movie S3) (AVI)

Back-projected cryo-ET reconstruction of immature virions pertaining to Figure 4C (Movie S4) (AVI)

Back-projected cryo-ET reconstruction of immature virions pertaining to Figure 4C (Movie S5) (AVI)

Back-projected cryo-ET reconstruction of IP6 stabilized intact cores pertaining to Figure 6A (Movie S6) (AVI)

Back-projected cryo-ET reconstruction of IP6 stabilized intact cores pertaining to Figure 6A (Movie S7) (AVI)

Back-projected cryo-ET reconstruction of IP6 stabilized intact cores pertaining to Figure 6A (Movie S8) (AVI)

Back-projected cryo-ET reconstruction of IP6 stabilized intact cores pertaining to Figure 6A (Movie S9) (AVI)

Back-projected cryo-ET reconstruction of IP6 stabilized compromised cores pertaining to Figure 6A (Movie S10) (AVI)

Back-projected cryo-ET reconstruction of IP6 stabilized compromised cores pertaining to Figure 6A (Movie S11) (AVI)

Back-projected cryo-ET reconstruction of LEN stabilized intact cores pertaining to Figure 6C (Movie S12) (AVI)

Back-projected cryo-ET reconstruction of LEN stabilized compromised cores pertaining to Figure 6C (Movie S13) (AVI)

Back-projected cryo-ET reconstruction of LEN stabilized compromised cores pertaining to Figure 6C (Movie S14) (AVI)

Back-projected cryo-ET reconstruction of LEN stabilized compromised cores pertaining to Figure 6C (Movie S15) (AVI)

Back-projected cryo-ET reconstruction of LEN stabilized compromised cores pertaining to Figure 6C (Movie S16) (AVI)

Back-projected cryo-ET reconstruction of intact conical core that retained iGFP and CDR markers in time-resolved studies, pertaining to Figure 7D (Movie S17) (MOV)

Back-projected cryo-ET reconstruction of tubular core that lost iGFP and retained CDR marker in time-resolved studies, pertaining to Figure 7G (Movie S18) (MOV)

Back-projected cryo-ET reconstruction of fully disassembled core that lost iGFP and CDR markers in time-resolved studies, pertaining to Figure 7J (Movie S19) (MOV)

Back-projected cryo-ET reconstruction of fully disassembled core that lost iGFP and CDR markers in time-resolved studies, pertaining to Figure 7M (Movie S20) (MOV)

Time-resolved fluorescence imaging, CLEM, and the locations of identified structures (Movie S21) (MP4)

Time-resolved fluorescence imaging of CDR loss and retention on INsfGFP-labeled HIV-1 cores immobilized on grids (corresponding to Figure 1B,C) (Movie S22) (MP4)

Differences in conventional and new workflows (Figure S1), including additional validation experiments/analysis of affinity capture, CLEM, and cryo-ET structures (Figures S1−S8), including associated legends (PDF)

Movies S1−S22 (PDF)

AUTHOR INFORMATION

Corresponding Authors

Gregory B. Melikyan − *Department of Pediatrics, Emory University School of Medicine, Atlanta, Georgia 30322, United States*; Email: gmeliki@emory.edu

Dmitry Lyumkis − *The Salk Institute for Biological Sciences, San Diego, California 92037, United States; Department of Molecular Biology, School of Biological Sciences, University of California, San Diego, California 92037, United States; Department of Integrative Structural and Computational Biology, The Scripps Research Institute, San Diego, California 92037, United States*; Email: dlyumkis@salk.edu

Ashwanth C. Francis − *Institute of Molecular Biophysics and Department of Biological Sciences, Florida State University, Tallahassee, Florida 32306, United States*; orcid.org/0000-0002-8663-2038; Email: acfrancis@fsu.edu

Authors

Zaida K. Rodriguez − *The Salk Institute for Biological Sciences, San Diego, California 92037, United States; Department of Molecular Biology, School of Biological Sciences, University of California, San Diego, California 92037, United States*

Jonathan R. Andino-Moncada − *Institute of Molecular Biophysics and Department of Biological Sciences, Florida State University, Tallahassee, Florida 32306, United States*

Sergey A. Buth − *Department of Pediatrics, Emory University School of Medicine, Atlanta, Georgia 30322, United States*

Atousa Mehrani − *The Salk Institute for Biological Sciences, San Diego, California 92037, United States*

Ahinsa Ranaweera − *Institute of Molecular Biophysics and Department of Biological Sciences, Florida State University, Tallahassee, Florida 32306, United States*

Jincheng Shi − *Institute of Molecular Biophysics and Department of Biological Sciences, Florida State University, Tallahassee, Florida 32306, United States*

Leonardo R. Andrade − *The Salk Institute for Biological Sciences, San Diego, California 92037, United States*

Satya Prakash Singh − *Institute of Molecular Biophysics and Department of Biological Sciences, Florida State University, Tallahassee, Florida 32306, United States*; orcid.org/0000-0001-8539-0295

Timothy S. Strutzenberg − *The Salk Institute for Biological Sciences, San Diego, California 92037, United States*

Mariana Marin − *Department of Pediatrics, Emory University School of Medicine, Atlanta, Georgia 30322, United States*

Ricardo Guerrero-Ferreira − *Robert P. Apkarian Integrated Electron Microscopy Core, Emory University School of Medicine, Atlanta, Georgia 30322, United States*

Hamid Rahmani − *Department of Integrative Structural and Computational Biology, The Scripps Research Institute, San Diego, California 92037, United States*

Danielle A. Grotjahn − *Department of Integrative Structural and Computational Biology, The Scripps Research Institute, San Diego, California 92037, United States*

Scott Stagg − *Institute of Molecular Biophysics and Department of Biological Sciences, Florida State University, Tallahassee, Florida 32306, United States*

Complete contact information is available at: https://pubs.acs.org/10.1021/acsnano.5c06724

Author Contributions

$^{\nabla}$Z.K.R., J.R.A.-M., and S.A.B. contributed equally. The manuscript was written by A.C.F., D.L., and G.B.M. through contributions of all authors. All authors have given approval to the final version of the manuscript. A.C.F. and G.B.M. conceived, designed, and developed the CLEM workflow. A.C.F., G.B.M., and D.L. designed experiments, provided supervision, and acquired funding resources. A.C.F., Z.K.R., J.R.A.-M., S.A.B., A.R., S.P.S., and M.M. evaluated the affinity capture protocol, from sample preparation through CLEM. A.C.F., Z.K.R., J.R.A.-M., S.A.B., and L.R.A. calculated the efficiency of the CLEM workflow. A.C.F., Z.K.R., J.R.A.-M., S.A.B., A.M., J.S., L.R.A., T.S.S., R.G., H.R., D.A.G., S.S., and D.L. assisted, collected, processed, and/or analyzed the CLEM and cryo-ET data sets.

Funding

This work was supported by the NIH/NIAID U54 AI170855 “Behavior of HIV in Viral Environment (B-HIVE)” HIV/AIDS Structural Biology Center to A.C.F., G.B.M., and D.L.; NIH/NIAID R01 AI129862 to G.B.M.; NIH/NIAID R01 AI150998, U01 AI136680, R01 AI184419, the Margaret T. Morris Foundation, and the Hearst Foundations to D.L.; NIH/NIAID 1R21AI174879 to A.C.F. and S.S.; National Institutes of Health F32GM148049 Fellowship and the Nomis Foundation Postdoctoral Fellowship to T.S.S.; and the Pioneer Fellowship to A.M. D.A.G. is supported by The Pew Scholars Program in the Biomedical Sciences and Scripps Research start-up funds. D.A.G. and D.L. are also grateful for pilot funding from the Irwin Jacobs Innovation and Collaboration Grant. Z.K.R. acknowledges the support of the Pathways in Biological Sciences (PiBS) NIH T32 Training Grant (T32 GM133351).

Notes

The authors declare no competing financial interest.

ACKNOWLEDGMENTS

We thank Dr. Elizabeth Wright and the members of her lab, including Drs. Zunlong Ke, Joshua Strauss, Rebecca Dillard, and Cheri Hampton, for assistance during the initial stages of this method development. We also thank Drs. Kenneth Taylor, Xiaofeng Fu, Hosna Rastegarpouyani, Ruizhi Peng, S. Shirin Kamalaldinezabadi, Behrouz, and Ms. Ananya Sengupta at FSU for training JA and AR and for assistance with sample freezing. We thank the Robert P. Apkarian Integrated Electron Microscopy Core Facility at Emory University School of Medicine (RRID: SCR_023537), the Biological Sciences Imaging Resource supported by Florida State University, and the Southeastern Center for Microscopy of Macro Molecular Machines (SECM4), NIH R24 GM145964, NIH S10 RR025080, and S10 RR024564. Some of this work was performed at the National Center for CryoEM Access and Training (NCCAT) and the Simons Electron Microscopy Center located at the New York Structural Biology Center, supported by the NIH Common Fund Transformative High-Resolution Cryo-Electron Microscopy program (U24 GM129539) and by grants from the Simons Foundation (SF349247) and the NY State Assembly. A portion of this research was supported by NIH grant R24GM154185 and performed at the Pacific Northwest Center for Cryo-EM (PNCC) with assistance from Craig Yoshioka, by the Waitt Advanced Biophotonics Core Facility of the Salk Institute (RRID:SCR_014838) with funding from NIH-NCI CCSG P30 CA014195, NIH-NIA San Diego Nathan Shock Center P30 AG068635, The Henry L. Guenther Foundation, and the Waitt Foundation. D.L. and D.A.G. acknowledge support from a Salk Collaboration Grant piloted by the Salk Cancer Center. T.S.S. acknowledges support from the National Institutes of Health Fellowship F32GM148049 and from the Nomis Foundation Postdoctoral Fellowship. A.M. was funded by the Pioneer Fellowship from the Salk Institute. ZKR acknowledges the support of the Pathways in Biological Sciences (PiBS) NIH T32 Training Grant (T32 GM133351).

ABBREVIATIONS

CLEM, correlative light and electron microscopy; fLM, fluorescence light microscopy; cryo-EM, cryogenic electron microscopy; cryo-TEM, cryogenic transmission electron microscopy; cryo-ET, cryogenic electron tomography; LMM, low-magnification montages; MMM, medium magnification montages; pA, protein-A from *Staphylococcus aureus*; CDR, Cyclophilin A−DsRed capsid marker; INsfGFP, integrase superfolder-green-fluorescent-protein; HXB2, HIV-1 strain from which the envelope was used.

REFERENCES

(1) Ganser-Pornillos, B. K.; Yeager, M.; Pornillos, O. Assembly and architecture of HIV. *Adv. Exp. Med. Biol.* **2012**, *726*, 441−465.

(2) de Marco, A.; Muller, B.; Glass, B.; Riches, J. D.; Krausslich, H. G.; Briggs, J. A. Structural analysis of HIV-1 maturation using cryo-electron tomography. *PLoS Pathog.* **2010**, *6* (11), No. e1001215.

(3) Briggs, J. A.; Wilk, T.; Welker, R.; Krausslich, H. G.; Fuller, S. D. Structural organization of authentic, mature HIV-1 virions and cores. *EMBO J.* **2003**, *22* (7), 1707−1715.

(4) Mattei, S.; Glass, B.; Hagen, W. J.; Krausslich, H. G.; Briggs, J. A. The structure and flexibility of conical HIV-1 capsids determined within intact virions. *Science* **2016**, *354* (6318), 1434−1437.

(5) Briggs, J. A.; Krausslich, H. G. The molecular architecture of HIV. *J. Mol. Biol.* **2011**, *410* (4), 491−500.

(6) Benjamin, J.; Ganser-Pornillos, B. K.; Tivol, W. F.; Sundquist, W. I.; Jensen, G. J. Three-dimensional structure of HIV-1 virus-like particles by electron cryotomography. *J. Mol. Biol.* **2005**, *346* (2), 577−588.

(7) Campbell, E. M.; Hope, T. J. HIV-1 capsid: The multifaceted key player in HIV-1 infection. *Nat. Rev. Microbiol.* **2015**, *13* (8), 471−483.

(8) Christensen, D. E.; Ganser-Pornillos, B. K.; Johnson, J. S.; Pornillos, O.; Sundquist, W. I. Reconstitution and visualization of HIV-1 capsid-dependent replication and integration in vitro. *Science* **2020**, *370* (6513), No. eabc8420.

(9) Sowd, G. A.; Shi, J.; Fulmer, A.; Aiken, C. HIV-1 capsid stability enables inositol phosphate-independent infection of target cells and promotes integration into genes. *PLoS Pathog.* **2023**, *19* (6), No. e1011423.

(10) Rasaiyaah, J.; Tan, C. P.; Fletcher, A. J.; Price, A. J.; Blondeau, C.; Hilditch, L.; Jacques, D. A.; Selwood, D. L.; James, L. C.; Noursadeghi, M.; et al. HIV-1 evades innate immune recognition through specific cofactor recruitment. *Nature* **2013**, *503* (7476), 402−405.

(11) Ganser-Pornillos, B. K.; Pornillos, O. Restriction of HIV-1 and other retroviruses by TRIM5. *Nat. Rev. Microbiol.* **2019**, *17* (9), 546−556.

(12) Shen, Q.; Kumari, S.; Xu, C.; Jang, S.; Shi, J.; Burdick, R. C.; Levintov, L.; Xiong, Q.; Wu, C.; Devarkar, S. C.; et al. The capsid lattice engages a bipartite NUP153 motif to mediate nuclear entry of HIV-1 cores. *Proc. Natl. Acad. Sci. U. S. A.* **2023**, *120* (13), No. e2202815120.

(13) Ni, T.; Zhu, Y.; Yang, Z.; Xu, C.; Chaban, Y.; Nesterova, T.; Ning, J.; Bocking, T.; Parker, M. W.; Monnie, C.; et al. Structure of native HIV-1 cores and their interactions with IP6 and CypA. *Sci. Adv.* **2021**, *7* (47), No. eabj5715.

(14) Rebensburg, S. V.; Wei, G.; Larue, R. C.; Lindenberger, J.; Francis, A. C.; Annamalai, A. S.; Morrison, J.; Shkriabai, N.; Huang, S. W.; KewalRamani, V.; et al. Sec24C is an HIV-1 host dependency factor crucial for virus replication. *Nat. Microbiol.* **2021**, *6* (4), 435−444.

(15) Francis, A. C.; Marin, M.; Singh, P. K.; Achuthan, V.; Prellberg, M. J.; Palermino-Rowland, K.; Lan, S.; Tedbury, P. R.; Sarafianos, S. G.; Engelman, A. N.; et al. HIV-1 replication complexes accumulate in nuclear speckles and integrate into speckle-associated genomic domains. *Nat. Commun.* **2020**, *11* (1), 3505.

(16) Achuthan, V.; Perreira, J. M.; Sowd, G. A.; Puray-Chavez, M.; McDougall, W. M.; Paulucci-Holthauzen, A.; Wu, X.; Fadel, H. J.; Poeschla, E. M.; Multani, A. S.; et al. Capsid-CPSF6 Interaction Licenses Nuclear HIV-1 Trafficking to Sites of Viral DNA Integration. *Cell Host Microbe* **2018**, *24* (3), 392−404.e8.

(17) Matreyek, K. A.; Yucel, S. S.; Li, X.; Engelman, A. Nucleoporin NUP153 phenylalanine-glycine motifs engage a common binding pocket within the HIV-1 capsid protein to mediate lentiviral infectivity. *PLoS Pathog.* **2013**, *9* (10), No. e1003693.

(18) Yoo, S.; Myszka, D. G.; Yeh, C.; McMurray, M.; Hill, C. P.; Sundquist, W. I. Molecular recognition in the HIV-1 capsid/cyclophilin A complex. *J. Mol. Biol.* **1997**, *269* (5), 780−795.

(19) Mamede, J. I.; Cianci, G. C.; Anderson, M. R.; Hope, T. J. Early cytoplasmic uncoating is associated with infectivity of HIV-1. *Proc. Natl. Acad. Sci. U. S. A.* **2017**, *114* (34), No. E7169−E7178.

(20) Francis, A. C.; Melikyan, G. B. Single HIV-1 Imaging Reveals Progression of Infection through CA-Dependent Steps of Docking at the Nuclear Pore, Uncoating, and Nuclear Transport. *Cell Host Microbe* **2018**, *23* (4), 536−548.E6.

(21) Gifford, L. B.; Melikyan, G. B. HIV-1 Capsid Uncoating Is a Multistep Process That Proceeds through Defect Formation Followed by Disassembly of the Capsid Lattice. *ACS Nano* **2024**, *18* (4), 2928−2947.

(22) Li, C.; Burdick, R. C.; Nagashima, K.; Hu, W. S.; Pathak, V. K. HIV-1 cores retain their integrity until minutes before uncoating in the nucleus. *Proc. Natl. Acad. Sci. U. S. A.* **2021**, *118* (10), No. e2019467118.

(23) Burdick, R. C.; Li, C.; Munshi, M.; Rawson, J. M. O.; Nagashima, K.; Hu, W. S.; Pathak, V. K. HIV-1 uncoats in the nucleus near sites of integration. *Proc. Natl. Acad. Sci. U. S. A.* **2020**, *117* (10), 5486−5493.

(24) Schifferdecker, S.; Zila, V.; Muller, T. G.; Sakin, V.; Anders-Osswein, M.; Laketa, V.; Krausslich, H. G.; Muller, B. Direct Capsid Labeling of Infectious HIV-1 by Genetic Code Expansion Allows Detection of Largely Complete Nuclear Capsids and Suggests Nuclear Entry of HIV-1 Complexes via Common Routes. *mBio* **2022**, *13* (5), No. e0195922.

(25) Francis, A. C.; Marin, M.; Shi, J.; Aiken, C.; Melikyan, G. B. Time-Resolved Imaging of Single HIV-1 Uncoating In Vitro and in Living Cells. *PLoS Pathog.* **2016**, *12* (6), No. e1005709.

(26) Burdick, R. C.; Morse, M.; Rouzina, I.; Williams, M. C.; Hu, W. S.; Pathak, V. K. HIV-1 uncoating requires long double-stranded reverse transcription products. *Sci. Adv.* **2024**, *10* (17), No. eadn7033.

(27) Guedan, A.; Donaldson, C. D.; Caroe, E. R.; Cosnefroy, O.; Taylor, I. A.; Bishop, K. N. HIV-1 requires capsid remodelling at the nuclear pore for nuclear entry and integration. *PLoS Pathog.* **2021**, *17* (9), No. e1009484.

(28) Deshpande, A.; Bryer, A. J.; Andino-Moncada, J. R.; Shi, J.; Hong, J.; Torres, C.; Harel, S.; Francis, A. C.; Perilla, J. R.; Aiken, C.; et al. Elasticity of the HIV-1 core facilitates nuclear entry and infection. *PLoS Pathog.* **2024**, *20* (9), No. e1012537.

(29) Bhattacharya, A.; Alam, S. L.; Fricke, T.; Zadrozny, K.; Sedzicki, J.; Taylor, A. B.; Demeler, B.; Pornillos, O.; Ganser-Pornillos, B. K.; Diaz-Griffero, F.; et al. Structural basis of HIV-1 capsid recognition by PF74 and CPSF6. *Proc. Natl. Acad. Sci. U. S. A.* **2014**, *111* (52), 18625−18630.

(30) Dostalkova, A.; Skach, K.; Kaufman, F.; Krizova, I.; Hadravova, R.; Flegel, M.; Ruml, T.; Hrabal, R.; Rumlova, M. PF74 and Its Novel Derivatives Stabilize Hexameric Lattice of HIV-1 Mature-Like Particles. *Molecules* **2020**, *25* (8), 1895.

(31) Rankovic, S.; Ramalho, R.; Aiken, C.; Rousso, I. PF74 Reinforces the HIV-1 Capsid To Impair Reverse Transcription-Induced Uncoating. *J. Virol.* **2018**, *92* (20), 10−128.

(32) Kelley, C. F.; Acevedo-Quinones, M.; Agwu, A. L.; Avihingsanon, A.; Benson, P.; Blumenthal, J.; Brinson, C.; Brites, C.; Cahn, P.; Cantos, V. D.; et al. Twice-Yearly Lenacapavir for HIV Prevention in Men and Gender-Diverse Persons. *N. Engl. J. Med.* **2025**, *392* (13), 1261−1276.

(33) Lynch, S.; Cohen, R. M.; Kavanagh, M.; Sharma, A.; Raphael, Y.; Pillay, Y.; Bekker, L. G. Lessons for long-acting lenacapavir: Catalysing equitable PrEP access in low-income and middle-income countries. *Lancet HIV* **2025**, S2352-3018(25)00161-4.

(34) Bester, S. M.; Wei, G.; Zhao, H.; Adu-Ampratwum, D.; Iqbal, N.; Courouble, V. V.; Francis, A. C.; Annamalai, A. S.; Singh, P. K.; Shkriabai, N.; et al. Structural and mechanistic bases for a potent HIV-1 capsid inhibitor. *Science* **2020**, *370* (6514), 360−364.

(35) Francis, A. C.; Di Primio, C.; Quercioli, V.; Valentini, P.; Boll, A.; Girelli, G.; Demichelis, F.; Arosio, D.; Cereseto, A. Second generation imaging of nuclear/cytoplasmic HIV-1 complexes. *AIDS Res. Hum. Retroviruses* **2014**, *30* (7), 717−726.

(36) Francis, A. C.; Cereseto, A.; Singh, P. K.; Shi, J.; Poeschla, E.; Engelman, A. N.; Aiken, C.; Melikyan, G. B. Localization and functions of native and eGFP-tagged capsid proteins in HIV-1 particles. *PLoS Pathog.* **2022**, *18* (8), No. e1010754.

(37) Siddiqui, M. A.; Saito, A.; Halambage, U. D.; Ferhadian, D.; Fischer, D. K.; Francis, A. C.; Melikyan, G. B.; Ambrose, Z.; Aiken, C.; Yamashita, M. A Novel Phenotype Links HIV-1 Capsid Stability to cGAS-Mediated DNA Sensing. *J. Virol.* **2019**, *93* (16), No. e00706-19.

(38) Xu, J. P.; Francis, A. C.; Meuser, M. E.; Mankowski, M.; Ptak, R. G.; Rashad, A. A.; Melikyan, G. B.; Cocklin, S. Exploring Modifications of an HIV-1 Capsid Inhibitor: Design, Synthesis, and Mechanism of Action. *J. Drug Des. Res.* **2018**, *5* (2), 1070.

(39) Huang, S. W.; Briganti, L.; Annamalai, A. S.; Greenwood, J.; Shkriabai, N.; Haney, R.; Armstrong, M. L.; Wempe, M. F.; Singh, S. P.; Francis, A. C.; et al. The primary mechanism for highly potent inhibition of HIV-1 maturation by lenacapavir. *PLoS Pathog.* **2025**, *21* (1), No. e1012862.

(40) Briganti, L.; Annamalai, A. S.; Bester, S. M.; Wei, G.; Andino-Moncada, J. R.; Singh, S. P.; Kleinpeter, A. B.; Tripathi, M.; Nguyen, B.; Radhakrishnan, R.; et al. Structural and mechanistic bases for resistance of the M66I capsid variant to lenacapavir. *mBio* **2025**, *16*, No. e0361324.

(41) Mallery, D. L.; Marquez, C. L.; McEwan, W. A.; Dickson, C. F.; Jacques, D. A.; Anandapadamanaban, M.; Bichel, K.; Towers, G. J.; Saiardi, A.; Bocking, T.; et al. IP6 is an HIV pocket factor that prevents capsid collapse and promotes DNA synthesis. *Elife* **2018**, *7*, No. e35335.

(42) Hampton, C. M.; Strauss, J. D.; Ke, Z.; Dillard, R. S.; Hammonds, J. E.; Alonas, E.; Desai, T. M.; Marin, M.; Storms, R. E.; Leon, F.; et al. Correlated fluorescence microscopy and cryo-electron tomography of virus-infected or transfected mammalian cells. *Nat. Protoc.* **2017**, *12* (1), 150−167.

(43) Schorb, M.; Gaechter, L.; Avinoam, O.; Sieckmann, F.; Clarke, M.; Bebeacua, C.; Bykov, Y. S.; Sonnen, A. F.; Lihl, R.; Briggs, J. A. G. New hardware and workflows for semi-automated correlative cryo-fluorescence and cryo-electron microscopy/tomography. *J. Struct. Biol.* **2017**, *197* (2), 83−93.

(44) Yu, G.; Vago, F.; Zhang, D.; Snyder, J. E.; Yan, R.; Zhang, C.; Benjamin, C.; Jiang, X.; Kuhn, R. J.; Serwer, P.; et al. Single-step antibody-based affinity cryo-electron microscopy for imaging and structural analysis of macromolecular assemblies. *J. Struct. Biol.* **2014**, *187* (1), 1−9.

(45) Schorb, M.; Briggs, J. A. Correlated cryo-fluorescence and cryo-electron microscopy with high spatial precision and improved sensitivity. *Ultramicroscopy* **2014**, *143*, 24−32.

(46) Metskas, L. A.; Briggs, J. A. G. Fluorescence-Based Detection of Membrane Fusion State on a Cryo-EM Grid using Correlated Cryo-Fluorescence and Cryo-Electron Microscopy. *Microsc. Microanal.* **2019**, *25* (4), 942−949.

(47) Jang, S.; Bedwell, G. J.; Singh, S. P.; Yu, H. J.; Arnarson, B.; Singh, P. K.; Radhakrishnan, R.; Douglas, A. W.; Ingram, Z. M.; Freniere, C.; et al. HIV-1 usurps mixed-charge domain-dependent CPSF6 phase separation for higher-order capsid binding, nuclear entry and viral DNA integration. *Nucleic Acids Res.* **2024**, *52*, 11060.

(48) Faysal, K. R.; Walsh, J. C.; Renner, N.; Marquez, C. L.; Shah, V. B.; Tuckwell, A. J.; Christie, M. P.; Parker, M. W.; Turville, S. G.; Towers, G. J.; et al. Pharmacologic hyperstabilisation of the HIV-1 capsid lattice induces capsid failure. *Elife* **2024**, *13*, No. e83605.

(49) Hübner, W.; Chen, P.; Del Portillo, A.; Liu, Y.; Gordon, R. E.; Chen, B. K. Sequence of human immunodeficiency virus type 1 (HIV-1) Gag localization and oligomerization monitored with live confocal imaging of a replication-competent, fluorescently tagged HIV-1. *J. Virol.* **2007**, *81* (22), 12596−12607.

(50) Jun, S.; Ke, D.; Debiec, K.; Zhao, G.; Meng, X.; Ambrose, Z.; Gibson, G. A.; Watkins, S. C.; Zhang, P. Direct visualization of HIV-1 with correlative live-cell microscopy and cryo-electron tomography. *Structure* **2011**, *19* (11), 1573−1581.

(51) Zila, V.; Margiotta, E.; Turonova, B.; Muller, T. G.; Zimmerli, C. E.; Mattei, S.; Allegretti, M.; Borner, K.; Rada, J.; Muller, B.; et al. Cone-shaped HIV-1 capsids are transported through intact nuclear pores. *Cell* **2021**, *184* (4), 1032−1046.e18.

(52) Wang, F.; Liu, Y.; Yu, Z.; Li, S.; Feng, S.; Cheng, Y.; Agard, D. A. General and robust covalently linked graphene oxide affinity grids for high-resolution cryo-EM. *Proc. Natl. Acad. Sci. U. S. A.* **2020**, *117* (39), 24269−24273.

(53) Wang, F.; Yu, Z.; Betegon, M.; Campbell, M. G.; Aksel, T.; Zhao, J.; Li, S.; Douglas, S. M.; Cheng, Y.; Agard, D. A. Amino and PEG-amino graphene oxide grids enrich and protect samples for high-resolution single particle cryo-electron microscopy. *J. Struct. Biol.* **2020**, *209* (2), 107437.

(54) Marquez, C. L.; Lau, D.; Walsh, J.; Shah, V.; McGuinness, C.; Wong, A.; Aggarwal, A.; Parker, M. W.; Jacques, D. A.; Turville, S.; et al. Kinetics of HIV-1 capsid uncoating revealed by single-molecule analysis. *Elife* **2018**, *7*, No. e34772.

(55) Kreysing, J. P.; Heidari, M.; Zila, V.; Cruz-Leon, S.; Obarska-Kosinska, A.; Laketa, V.; Rohleder, L.; Welsch, S.; Kofinger, J.; Turonova, B.; et al. Passage of the HIV capsid cracks the nuclear pore. *Cell* **2025**, *188* (4), 930−943 E21.

(56) Hou, Z.; Shen, Y.; Fronik, S.; Shen, J.; Shi, J.; Xu, J.; Chen, L.; Hardenbrook, N.; Thompson, C.; Neumann, S.et al. Correlative In Situ Cryo-ET Reveals Cellular and Viral Remodeling Associated with Selective HIV-1 Core Nuclear Import, *bioRxiv*, **2025**,

(57) Li, C.; Burdick, R. C.; Siddiqui, R.; Janaka, S. K.; Hsia, R. C.; Hu, W. S.; Pathak, V. K. Lenacapavir disrupts HIV-1 core integrity while stabilizing the capsid lattice. *Proc. Natl. Acad. Sci. U. S. A.* **2025**, *122* (14), No. e2420497122.

(58) Sood, C.; Francis, A. C.; Desai, T. M.; Melikyan, G. B. An improved labeling strategy enables automated detection of single-virus fusion and assessment of HIV-1 protease activity in single virions. *J. Biol. Chem.* **2017**, *292*, 20196.

(59) McGuinness, C.; Walsh, J. C.; Bayly-Jones, C.; Dunstone, M. A.; Christie, M. P.; Morton, C. J.; Parker, M. W.; Bocking, T. Single-molecule analysis of the entire perfringolysin O pore formation pathway. *Elife* **2022**, *11*, No. e74901.

(60) Fuest, M.; Schaffer, M.; Nocera, G. M.; Galilea-Kleinsteuber, R. I.; Messling, J. E.; Heymann, M.; Plitzko, J. M.; Burg, T. P. In situ Microfluidic Cryofixation for Cryo Focused Ion Beam Milling and Cryo Electron Tomography. *Sci. Rep.* **2019**, *9* (1), 19133.

(61) Pizzato, M.; Erlwein, O.; Bonsall, D.; Kaye, S.; Muir, D.; McClure, M. O. A one-step SYBR Green I-based product-enhanced reverse transcriptase assay for the quantitation of retroviruses in cell culture supernatants. *J. Virol. Methods* **2009**, *156* (1−2), 1−7.

(62) Heiligenstein, X.; Paul-Gilloteaux, P.; Raposo, G.; Salamero, J. eC-CLEM: A multidimension, multimodel software to correlate intermodal images with a focus on light and electron microscopy. *Methods Cell Biol.* **2017**, *140*, 335−352.

(63) Mastronarde, D. N. Automated electron microscope tomography using robust prediction of specimen movements. *J. Struct. Biol.* **2005**, *152* (1), 36−51.

(64) Eisenstein, F.; Yanagisawa, H.; Kashihara, H.; Kikkawa, M.; Tsukita, S.; Danev, R. Parallel cryo electron tomography on in situ lamellae. *Nat. Methods* **2023**, *20* (1), 131−138.

(65) Francis, A. C.; Marin, M.; Prellberg, M. J.; Palermino-Rowland, K.; Melikyan, G. B. HIV-1 Uncoating and Nuclear Import Precede the Completion of Reverse Transcription in Cell Lines and in Primary Macrophages. *Viruses* **2020**, *12* (11), 1234.

(66) Scheres, S. H. RELION: Implementation of a Bayesian approach to cryo-EM structure determination. *J. Struct. Biol.* **2012**, *180* (3), 519−530.

(67) Zheng, S.; Wolff, G.; Greenan, G.; Chen, Z.; Faas, F. G. A.; Barcena, M.; Koster, A. J.; Cheng, Y.; Agard, D. A. AreTomo: An integrated software package for automated marker-free, motion-corrected cryo-electron tomographic alignment and reconstruction. *J. Struct. Biol. X* **2022**, *6*, 100068.

(68) Bykov, Y. S.; Cohen, N.; Gabrielli, N.; Manenschijn, H.; Welsch, S.; Chlanda, P.; Kukulski, W.; Patil, K. R.; Schuldiner, M.; Briggs, J. A. G. High-throughput ultrastructure screening using electron microscopy and fluorescent barcoding. *J. Cell Biol.* **2019**, *218* (8), 2797−2811.

(69) Bykov, Y. S.; Cortese, M.; Briggs, J. A.; Bartenschlager, R. Correlative light and electron microscopy methods for the study of virus-cell interactions. *FEBS Lett.* **2016**, *590* (13), 1877−1895.